ELEMENTA
Science of the Anthropocene

Heinemann, G, et al. 2022. Evaluation of simulations of near-surface variables using the regional climate model CCLM for the MOSAiC winter period. *Elem Sci Anth*, 10: 1. DOI: https://doi.org/10.1525/elementa.2022.00033

RESEARCH ARTICLE

Evaluation of simulations of near-surface variables using the regional climate model CCLM for the MOSAiC winter period

Günther Heinemann[1,*], Lukas Schefczyk[2], Sascha Willmes[1], and Matthew D. Shupe[3,4]

The ship-based experiment MOSAiC 2019/2020 was carried out during a full year in the Arctic and yielded an excellent data set to test the parameterizations of ocean/sea-ice/atmosphere interaction processes in regional climate models (RCMs). In the present paper, near-surface data during MOSAiC are used for the verification of the RCM COnsortium for Small-scale MOdel–Climate Limited area Mode (COSMO-CLM or CCLM). CCLM is used in a forecast mode (nested in ERA5) for the whole Arctic with 15 km resolution and is run with different configurations of sea ice data. These include the standard sea ice concentration taken from passive microwave data with around 6 km resolution, sea ice concentration from Moderate Resolution Imaging Spectroradiometer (MODIS) thermal infrared data and MODIS sea ice lead fraction data for the winter period. CCLM simulations show a good agreement with the measurements. Relatively large negative biases for temperature occur for November and December, which are likely associated with a too large ice thickness used by CCLM. The consideration of sea ice leads in the sub-grid parameterization in CCLM yields improved results for the near-surface temperature. ERA5 data show a large warm bias of about 2.5°C and an underestimation of the temperature variability.

Keywords: Arctic, Sea ice, Regional climate model, Verification, Leads, MODIS

1. Introduction

Regional climate models (RCMs) are an important tool to understand the recent and future climate change in the Arctic. Parameterization of the stable boundary layer (SBL) and sub-grid processes such as leads are major challenges for atmospheric models. In most state-of-the-art RCMs, leads are not realistically represented. Sea ice is considered as a mean concentration over a model grid box, and surface fluxes are computed according to the fractions of water and ice. Most uncoupled RCMs assume open water for the water fraction, which is unrealistic during winter, where leads and polynyas are almost totally covered with thin ice very rapidly (Preußer et al., 2019). The thin ice coverage has a large effect on the surface fluxes and sea ice production (Gutjahr et al., 2016).

Recent RCM intercomparison studies for the Arctic were shown by Sedlar et al. (2020) and Inoue et al. (2020). Both studies are for the Arctic summer in 2014. Inoue et al. (2020) compared RCM data with a focus on radiation and clouds for the ice-free ocean. Sedlar et al. (2020) used measurements in the marginal ice zone with only weak energy fluxes for the comparison of boundary layer processes. A study for wintertime conditions is shown by Heinemann et al. (2021) for a 4-week drift of an icebreaker in the inner Arctic in 2019.

In the present paper, we use near-surface meteorological data from the MOSAiC experiment during November 2019 to April 2020, where the German research vessel "Polarstern" drifted with the ice in the inner Arctic (Shupe et al., 2022). A meteorological tower was installed on the sea ice, and atmospheric remote sensing measurements as well as radiosonde ascents were performed on the ship (Shupe et al., 2022). The data are used for a verification of the RCM COnsortium for Small-scale MOdel–Climate Limited area Mode (COSMO-CLM or CCLM) with a horizontal resolution of 15 km (**Figure 1**). The sea-ice concentration (SIC) data are from Advanced Microwave Scanning Radiometer (AMSR2) data (Spreen et al., 2008). In addition, the impact of considering SIC and sea ice leads from Moderate Resolution Imaging Spectroradiometer (MODIS) data (Willmes and Heinemann, 2016) is investigated. In contrast to previous studies like Heinemann et al. (2021), we can study the model performance for a whole winter season with an unprecedented suite of measurements.

[1] Environmental Meteorology, University of Trier, Trier, Germany

[2] State Environment Agency Rhineland-Palatinate, Mainz, Germany

[3] Cooperative Institute for Research in Environmental Sciences, University of Colorado, Boulder, CO, USA

[4] NOAA Physical Sciences Laboratory, Boulder, CO, USA

* Corresponding author:
Email: heinemann@uni-trier.de

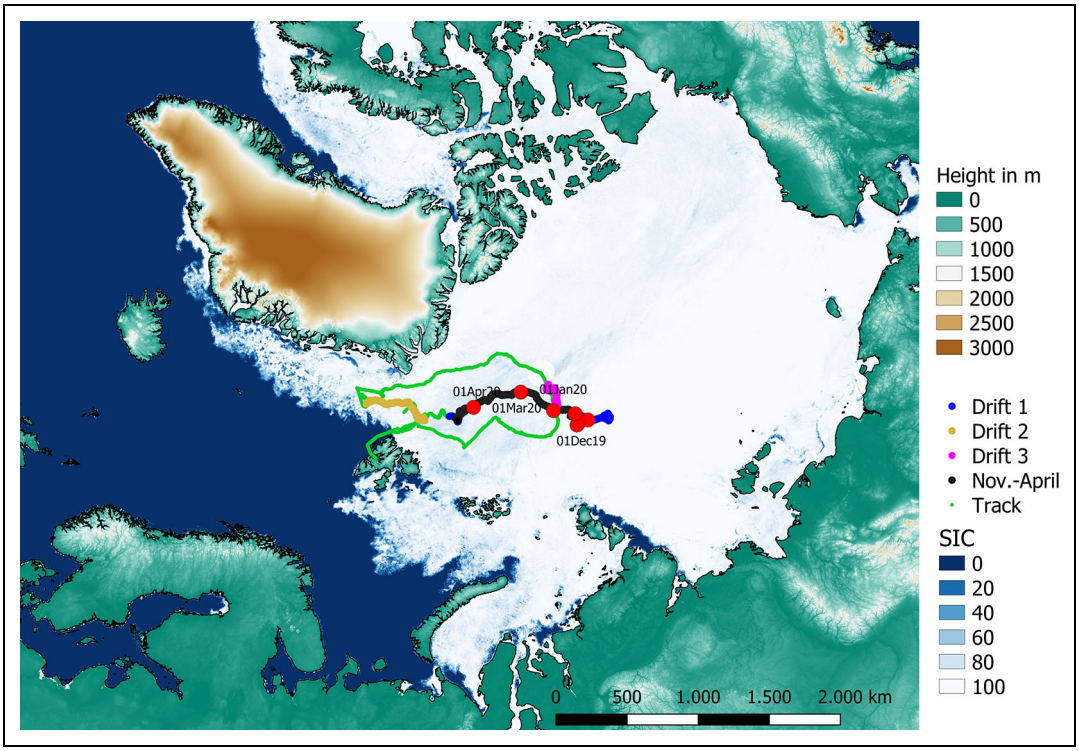

Figure 1. Model domain of the CCLM model. Model domain with 15 km resolution with topography and AMSR2 sea ice concentration for April 23, 2020. The green line shows the entire track of Polarstern, the 3 drift phases are marked in blue, orange, and violet. The black line marks the winter period November to April with dates of selected ship positions.

2. Model and data

2.1. MOSAiC data

During the MOSAiC experiment, comprehensive measurements of the atmospheric boundary layer (ABL) were performed during a full year in the Arctic. The German research icebreaker Polarstern was the base of this experiment, and during the first phase of the experiment Polarstern drifted from the northern Laptev Sea with the transpolar drift almost to Svalbard (October 2019 to mid-May 2020; **Figure 1**). The drift was interrupted due to logistic reasons (with a stay near Longyearbyen, Svalbard, from June 4 to 8, 2020) and the necessity to relocate the drift position, and new drift phases took place from middle of June to end of July and end of August to end of September 2020 (see Shupe et al., 2022, for details). During the drift phases, a central observatory was installed on the sea ice within about 2 km of Polarstern. Part of this observatory was "Met City," which was at a distance of 300–600 m from the ship and hosted a large number of measurement systems. In the present study, we focus on the near-surface measurements made at a 10-m-tower and a radiation station at Met City and the measurements from the Polarstern meteorological system. An overview of measurements relevant for the present study is given in **Tables 1** and **2**. The measurements from Polarstern are available continuously for the whole period, while the Met City data have gaps due to the relocations of the observatory (**Table 2**). There are additional data for the period between mid-May and mid-June at the MOSAiC ice floe, when a remote station was installed in the central observatory while Polarstern was gone (Shupe et al., 2022). However, these data are not used for the present study since we focus on the winter period from November to April.

2.2. CCLM

The model used for this study is the nonhydrostatic RCM COSMO-CLM or CCLM (Rockel et al., 2008; Steger and Bucchignani, 2020, available at https://clmcom.scrollhelp.site/clmcommunity). CCLM has been used for several studies of air/sea-ice/ocean interactions and boundary layer processes in polar regions (e.g., Bauer et al., 2013; Gutjahr et al., 2016; Kohnemann and Heinemann, 2021). Verification studies for CCLM have been performed, for example, using standard weather station data (Kohnemann et al., 2017; Platonov and Kislov, 2020), radiosondes (Souverijns et al., 2019; Zentek and Heinemann, 2020), and aircraft data for the katabatic wind over Greenland (Heinemann, 2020). For the present paper, CCLM is used with a horizontal resolution of about 15 km for the whole Arctic (C15; **Figure 1**). C15 took part in two CORDEX model intercomparison studies in the Arctic using ship-based measurements during summer (Inoue et al., 2020; Sedlar et al., 2020).

Initial and boundary data are taken from ERA5 (Hersbach et al., 2020) with hourly resolution (**Table 3**). The model is used in a forecast mode (reinitialized daily at 18 UTC, spin-up time of 6 h) for October 2019 to September 2020 (the period of the MOSAiC experiment). No nudging is performed during the run. Model output is available every 1 h. In the vertical, the model extends up to

Table 1. MOSAiC measurements from Polarstern meteorological system (Knust, 2017) (data provider: AWI)

Quantity	Instrument	Height, Position
Temperature and humidity	HMP 155 (Vaisala, Finland) mounted in radiation shield, not ventilated	29 m (portside and starboard)
Wind speed and direction	2D-sonic (Thies, Germany)	39 m (portside and starboard)
Cloud ceiling	Cloud ceilometer CL51 (Vaisala, Finland)	20 m (portside, maximum range of 15,000 m)
Water temperature	PT-100 (Thies, Germany)	–5 m (portside and starboard)
Global radiation	Pyranometer (CM11, Kipp & Zonen, Netherlands)	34 m (crow's nest)
Visibility	FS11 (Vaisala, Finland)	20 m (portside, maximum range of 75,000 m)
Pressure	Electronic barometer (SETRA B270, Setra Systems Inc., USA)	16 m (reduced to sea level)
Precipitation	SRM 450 (Eigenbrodt, Germany)	34 m (crow's nest)
Data availability	October 1, 2019, to September 30, 2020	

Table 2. MOSAiC measurements from Met City including the 10-m tower (Cox et al., 2021) and the radiation station (Riihimaki, 2021; data provider: 1: University of Colorado/NOAA, or 2: U.S. DOE ARM program)

Quantity	Instrument	Height (Nominal)
Temperature and humidity[1]	Vaisala PTU307 (2 m), and HMT337 (6, 10 m)	2, 6, and 10 m
Wind speed and direction[1]	3D-sonic (Metek, Germany) u-Sonic Cage MP	2, 6, and 10 m
Turbulent fluxes[1]	3D-sonic (Metek, Germany) u-Sonic Cage MP	2, 6, and 10 m
Surface temperature[2]	Derived from up- and down-looking Eppley Laboratory Precision Infrared Radiometer (assumed emissivity of 0.985)	3 m
Radiation (4 components)[2]	Eppley Laboratory Precision Infrared Radiometer (PIR) and Precision Spectral Pyranometer (PSP), both up- and down-looking	3 m (down-looking), 1 m (up-looking)
Data availability	October 15, 2019, to May 10, 2020, June 24 to July 29, 2020, August 29 to September 18, 2020	

Table 3. Configuration of the CCLM simulations

Forcing	Vertical/Horizontal Resolutions, Lowest 3 Levels	Run Mode	Sea Ice Concentration (SIC) and Thickness
ERA5	60 levels, 14 km 5, 16, and 31 m	Forecast mode (reinitialized at 18 UTC, 6-h spin-up)	AMSR2 and MODIS (SIC) PIOMAS, daily data
Run name	**SIC and thin ice thickness**		
C15	AMSR2 SIC, "pole hole" filled with SIC = 100%		
C15MOD	MODIS SIC with gap filling by AMSR2 data		
C15MOD0	SIC computed from 12-km lead fraction (LF) taking SIC = 0 for leads with gap filling by C15MOD data		
C15MOD0h	As C15MOD0, but assuming that half of the LF area has SIC = 0		
C15MOD0htit	As C15MOD0h, but with doubled sub-grid-scale thin ice thickness		

22 km with 60 vertical levels; 12 levels are below 500 m in order to obtain a high resolution of the boundary layer. The first model level is at 5 m above the surface. Sea ice concentration as shown in **Figure 1** is taken as daily data from an AMSR2 dataset with 6 km resolution (Spreen et al., 2008). In addition, daily SIC and information about sea ice leads are taken from MODIS data for November 2019 to April 2020 (see **Table 3** and Section 2.3). Sea ice

Table 4. Characteristics and parameterizations of the sea ice model used in CCLM

Sea Ice Physics	Parameterization	References
Thin ice (0.01–0.2 m)	No snow layer	Schröder et al. (2011)
Thick ice (>0.2 m)	Variable snow layer (10% of the ice thickness)	Heinemann et al. (2021)
Penetration of solar radiation	In snow and ice layer	Perovich (2007)
Temperature gradients in ice and snow	Nonlinear depending on layer thickness	Mironov et al. (2012)
Albedo	Modified Køltzow scheme, depending on temperature and ice thickness (including a melt pond parameterization)	Køltzow (2007), Gutjahr et al. (2016)
Grid-scale ice thicknesses	SIC > 0.7: PIOMAS SIC $\leq$ 0.7: depending on temperature and SIC	Zhang and Rothrock (2003), Heinemann et al. (2021)
Sub-grid-scale thin ice in leads and polynyas	Variable, computed from thermodynamic ice growth with a bulk approach over a time period of 24 h for polynyas (SIC $\leq$ 0.7) and 6 h for leads (SIC > 0.7), respectively.	Heinemann et al. (2021)

Table 5. Boundary layer parameterizations in CCLM

Roughness Lengths	Parameterization	References
Ocean	Modified Charnock relation	Charnock (1955)
Sea ice	Roughness length for momentum (z_0): dependent on ice thickness and SIC; roughness length for heat (z_T): ratio z_T/z_0 dependent on roughness Reynolds number, form drag	Andreas (1987), Weiss et al. (2011), Lüpkes and Gryanik (2015), Elvidge et al. (2016)
SBL		
Minimum diffusion coefficients	0.01 m^2/s	Zentek and Heinemann (2020), Heinemann (2020)
Asymptotic mixing length	Depending on TKE and stability	Hebbinghaus and Heinemann (2006)
Tile approach for sea ice		
Surface classes	Grid-scale ice (all thicknesses $\geq$1 cm), sub-grid-scale thin ice (1–20 cm), open ocean	Heinemann et al. (2021)

thickness is prescribed daily from interpolated Pan-Arctic Ice Ocean Modeling and Assimilation System (PIOMAS) fields (Zhang and Rothrock, 2003). Topography data are taken from Hastings and Dunbar, 1999. A full technical documentation of the CCLM model is given in Zentek (2019). Modifications were introduced in CCLM for the SBL, which improve the simulations of the surface inversion over ice surfaces (Zentek and Heinemann, 2020; Heinemann, 2020). One main modification was the reduction of the minimal values of the diffusion coefficients for heat and momentum from originally 0.4 m^2/s to 0.01 m^2/s. The cloud schemes are described in Doms et al. (2013). The cloud schemes include cloud water, cloud ice, rain, snow, and graupel as 3-dimensional prognostic variables using a bulk microphysics parameterization scheme. The radiative transfer scheme (Ritter and Geleyn, 1992) is based on a δ-2-stream solution of the radiative transfer equation and is solved for 8 spectral intervals for each model layer considering cloud water droplets, cloud ice crystals, water vapor, ozone, carbon dioxide, and other minor trace gases as well as aerosols (Doms et al., 2013).

CCLM was adapted to polar regions by implementing a 2-layer sea ice model (**Table 4**) and a tile approach for sea ice (Gutjahr et al., 2016; Heinemann et al., 2021). The tile approach includes the parameterization of the sub-grid-scale ice thickness (thin ice in leads and polynyas), a parameterization of the sea ice form drag (Lüpkes and Gryanik, 2015) and parameterizations for the roughness length of heat according to Andreas (1987), see **Table 5**. These parameterizations are the same as in Heinemann et al. (2021), the only difference is that a different roughness length parameterization for thick ice is used. Since the roughness length proposed by Weiss et al. (2011) for closed pack ice resulted in an underestimation of the wind speed (Heinemann et al., 2021), we choose for closed thick pack ice a value of 2.5×10^{-3} for the drag coefficient as proposed by Elvidge et al. (2016), which corresponds to a value for the roughness length of 3.3 mm.

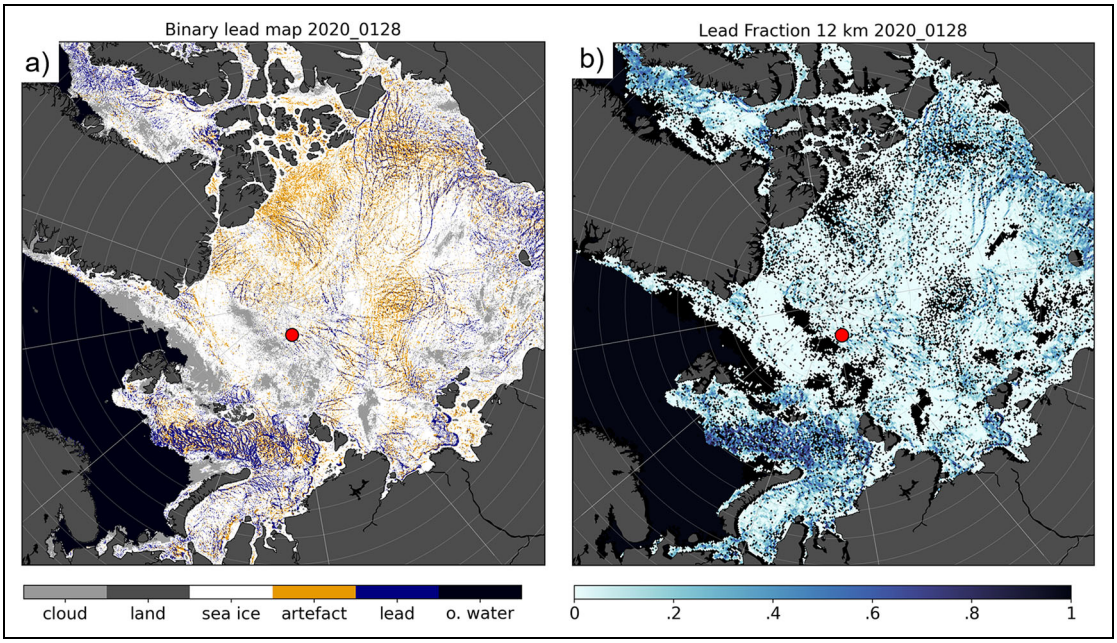

Figure 2. MODIS lead retrievals January 28, 2020. (a) Sea ice lead map (1 km resolution) for January 28, 2020, from MODIS thermal infrared data (blue/orange: lead pixels with high/lower detection certainty); (b) lead fraction with 12 km resolution for January 28, 2020. The position of Polarstern is indicated by a red dot.

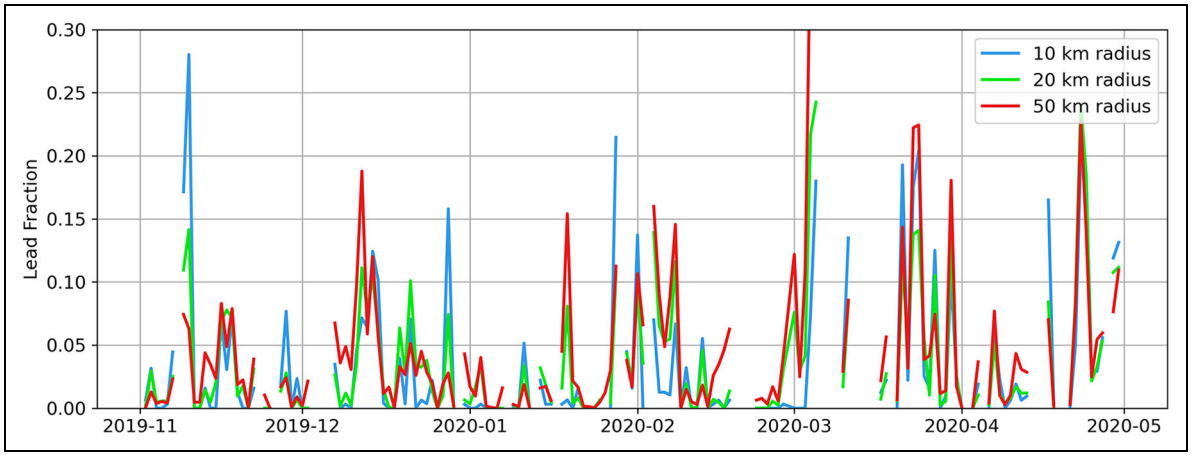

Figure 3. Daily lead fraction from MODIS data along the Polarstern drift. Daily lead fraction from MODIS data for November 2019 to April 2020 along the Polarstern drift within a radius of 10, 20, and 50 km.

2.3. MODIS data

2.3.1. MODIS leads retrieval

We use daily binary lead maps that are derived from MODIS thermal infrared imagery (Reiser et al., 2020). In this dataset, a lead is considered as a significant local surface temperature anomaly with respect to the surrounding thick sea ice. As such, depending on lead width, both open water and thin ice covered lead pixels are automatically detected at a spatial resolution of 1 km^2. False classifications due to thermal signatures of unidentified clouds and classifications with high uncertainty are filtered out using a fuzzy approach and marked as artifacts (Willmes and Heinemann, 2016).

Figure 2 shows an example of the distribution of leads for January 28, 2020. The high-resolution lead map (**Figure 2a**) shows that leads are ubiquitous in the inner pack ice, and some leads extend over distances of 200 km and more in length, but their width is on a kilometer scale or less. The leads detected in the lead retrieval with 1 km resolution may have a scale of less than 1 km, as long their thermal signal is strong enough (an example is shown in Figure S1). For the use in the CCLM model, a lead fraction (LF) distribution with 12 km resolution was calculated (**Figure 2b**). The thermal signature of leads used in the retrieval is also associated with very strong exchange of heat and moisture between the relatively warm ocean and the cold winter atmosphere, leading to a warming of the ABL (Lüpkes et al., 2008).

The lead fraction around Polarstern is shown in **Figure 3** for a radius of 10 km, 20 km, and 50 km. The gaps occur for days when there is no coverage by MODIS data because of clouds or due to the filtering of lead pixels with

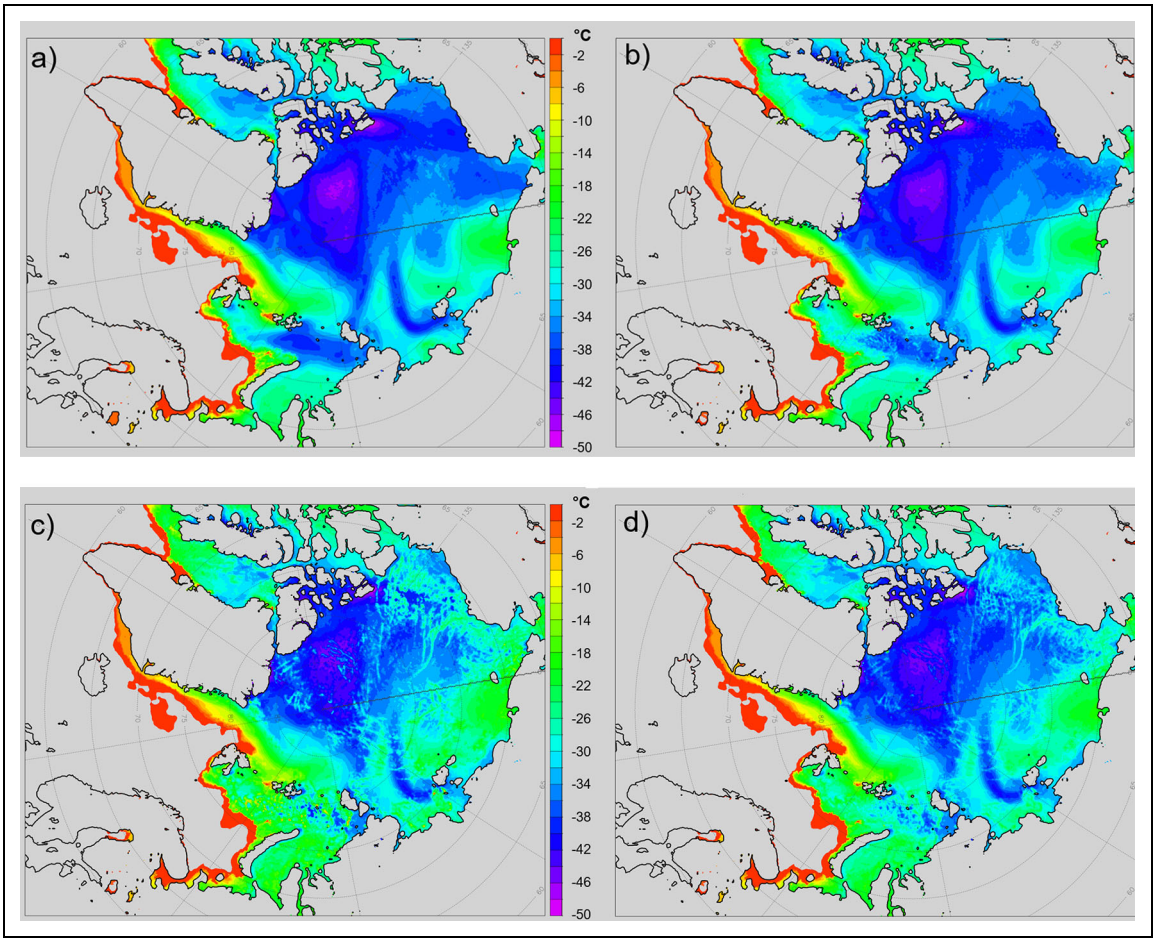

Figure 4. Simulated surface temperature for January 28, 2020. Daily mean of the simulated surface temperature with different sea ice concentration data sets for January 28, 2020 from (a) the C15 reference run (AMSR2 data), (b) the C15MOD run, (c) the C15MOD0 run, and (d) the C15MOD0h run.

high uncertainty. Within a 10 km radius, which is approximately the C15 grid size, lead fractions reach 10% on many days, on a few days even 20% is reached. The same holds for the larger radii of 20 km and 50 km, which are more typical for the effective resolution of CCLM due to the numerical discretization (Zentek et al., 2016). For some days, the lead fractions for the larger radii are higher than for the smaller radius, which suggests that heat advection from the surrounding grid points may also affect the Polarstern grid point.

2.3.2. MODIS SIC retrieval

The MODIS lead product provides information about the sea-ice surface that can be transformed into an alternative sea-ice concentration boundary field for the simulations that exceeds the spatial resolution of passive microwave products. Given that during winter, regions of low ice concentration in the central pack are caused by leads we can convert the MODIS lead maps to a MODIS sea-ice concentration product. Therefore, we consider the SIC to be 100% where no lead is present and calculate SIC within leads based on the tie-points of the freezing temperature of sea water (−1.8°C) and the surface temperature of the surrounding thick ice (Drüe and Heinemann, 2004). AMSR2 data are used for filling the gaps in the MODIS SIC field.

Different C15 runs have been performed using SIC from AMSR2 and MODIS data (see **Table 3**): The reference run (C15) uses AMSR2 SIC, a second run (C15MOD) uses the SIC from the merged MODIS/AMSR SIC, and a third run (C15MOD0) uses the lead fraction (LF) map in addition, where leads are considered to be ice-free in the initial field for CCLM. In a fourth run (C15MOD0h), we assume that only half of the LF area is ice-free in the initial field for CCLM. This is motivated by the fact that the area of sub-grid-scale thin ice is overestimated when using LF, since there are many leads smaller in width than the MODIS resolution. Leads are considered in the sub-grid sea ice parameterization in CCLM, and the thin ice thickness for each pixel is computed by thermodynamic growth during the daily initialization of the sea ice model (see **Table 4**). In a fifth run (C15MOD0htit), the same SIC as in C15MOD0h is used, but with doubled thin ice thickness in leads.

The effect of the different sea ice concentration fields on the simulated surface temperature is demonstrated in **Figure 4** for an example on January 28, 2020. The C15MOD run (**Figure 4b**) shows some warmer spots compared to the reference run (e.g., in the Kara Sea), but the

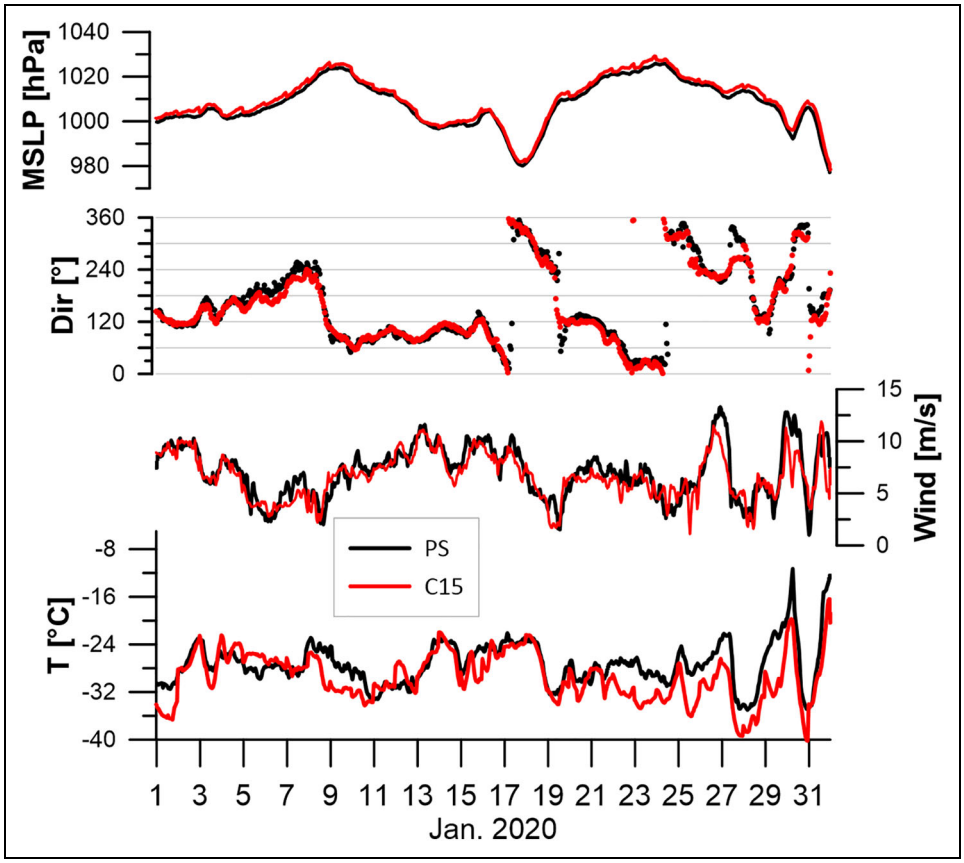

Figure 5. Near-surface quantities from simulations and Polarstern measurements for January 2020. Mean sea level pressure (top panel), temperature (lower panel), and wind speed and direction (middle panels) for January 2020 for the Polarstern observations (1 h values, levels at 29 and 39 m for temperature and wind, respectively, black) and C15 simulations at 31 m (1 h values, red).

impact is small for most areas. This results from the fact that the SIC in leads in the MODIS data is larger than 90% in most cases and there is only a small fraction of sub-grid thin ice in the C15 grid box. This fraction increases if the leads are considered to be ice-free when calculating the grid-scale sea ice concentration in the C15MOD0 run (**Figure 4c**) and C15MOD0h run (**Figure 4d**). In this case, the leads are better considered in the sub-grid-scale parameterization (see **Figure 2**), and temperatures are slightly lower in the C15MOD0h run because of the reduced area of thin ice. The thin-ice thickness in leads varies between 1 cm and 15 cm for this example (not shown). Temperatures for the C15MOD0htit run (Figure S2a) are similar to the C15MOD0h run.

The composite of MODIS ice surface temperature (IST) data on January 28, 2020 (Figure S2b) shows good agreement for the broad temperature distribution. However, the IST product used here (Hall and Riggs, 2021), which has an accuracy of about 2°C (Hall et al., 2004), contains many pixels that are contaminated by clouds leading to artifacts in the IST data. In addition, the composite of MODIS IST is not a real average, since this is an overlay of all satellite swaths with IST values at different times. There is also a sampling problem with respect to satellite swath times and cloud-free conditions. In contrast, the method for detecting sea-ice leads used in the present paper uses an additional cloud filter, which removes most artifacts. A quantitative comparison between MODIS IST and CCLM IST as shown in Heinemann et al. (2021) would require additional filtering of MODIS data and selecting cloud-free grid points in CCLM, which is beyond the scope of the present study.

Since the C15MOD/C15MOD0h runs are very similar to the C15/C15MOD0htit runs, we focus on the comparison of the C15, C15MOD0, and C15MOD0h runs in the following.

3. Results

3.1. Comparison of CCLM simulations with Polarstern observations

3.1.1. Case studies for selected periods

The measurements of the wind at 39 m and the temperature at 29 m for January 2020 are shown in **Figure 5** together with the simulation results at the 31-m level. Wind speeds are moderate most of the time, but for the end of January the wind speed exceeds 10 m/s associated with cyclonic events. The measurements show variations on the sub-daily scale, which are most pronounced during frontal passages (e.g., January 18, 27, and 30). The temperatures drop below −30°C during these events, which were followed by warming periods. Wind directions show also remarkable changes during the passage of cyclones

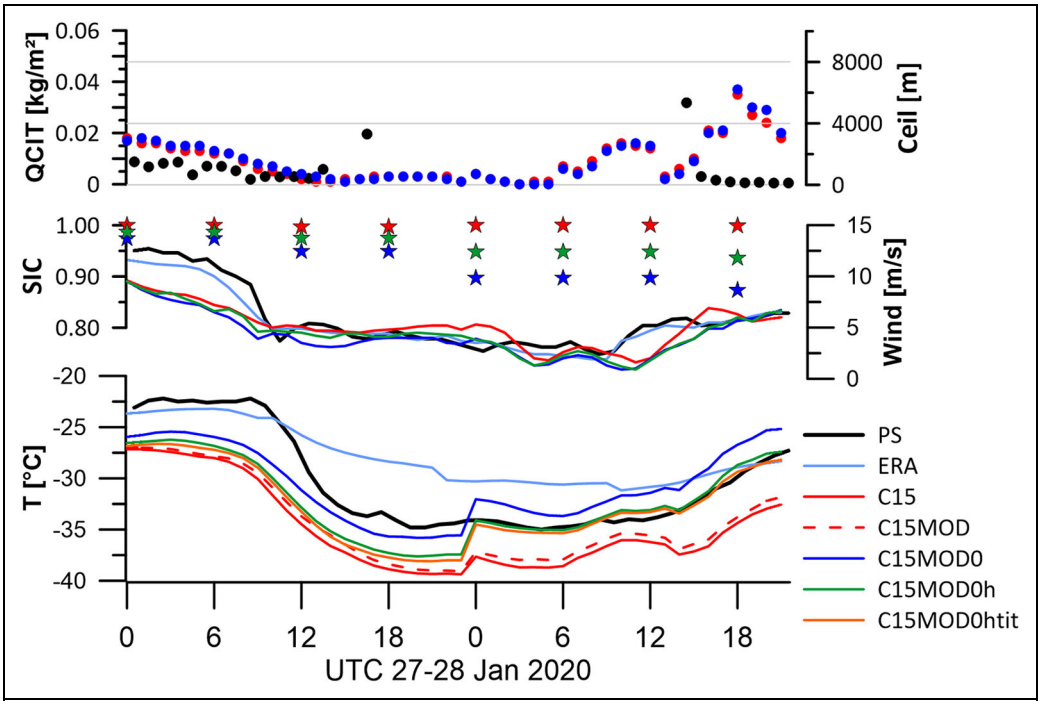

Figure 6. Near-surface quantities from simulations and Polarstern measurements for January 27 and 28, 2020. Measured and simulated quantities at Polarstern for January 27 and 28, 2020. Polarstern observations for temperature and wind were at 29 m and 39 m, respectively (black), CCLM simulations (different colors, see **Table 3** for different setups of the runs) for temperature and wind are taken at 31 m. Lower panel: temperature; middle panel: wind speed (lines) and SIC (stars); upper panel: sum of the total integrated cloud water and cloud ice content (QCIT) of the simulations (only for C15 [red dots] and C15MOD0 [blue dots]) and measured cloud base height (Ceil, black dots). ERA5 data (light blue) for the 2-m temperature and 10-m wind are shown for comparison. All data are 1h-values (SIC data shown only every 6 h).

and frontal systems. The simulations agree very well with the measurements for pressure, wind speed and direction. Too low temperatures are simulated particularly for cooling periods with relatively low wind speeds.

We will now look at the cooling event occurring on January 27 and 28 in more detail. A map of mean sea level pressure (MSLP), 2-m temperature and wind for January 27 is presented in Figure S3, which shows Polarstern in a warm sector prior to the passage of a cold front. The start of the cooling event is observed at about 10 UTC on January 27 (**Figure 6**), when the temperature drops from about –22°C to about –35°C. This is associated with a drop of the wind speed below 5 m/s. The temperature stays near –35°C for about 18 h and begins to rise in the second half of January 28. The cloud base observations show low clouds before the cooling event and no clouds in the lowest 10 km during the cold phase. Very low cloud base heights are observed in the second half of January 28. As a measure of the presence of clouds in the simulations, we take the sum of the total integrated cloud water and cloud ice content (QCIT). In agreement with the observations, the simulations show very low QCIT during the cooling event and the next 18 h, but some clouds between 06 and 12 UTC on January 28, when the observations indicate cloud-free conditions. In the CCLM simulations, the temperature drop is similar as in the observations, but all simulations are too cold prior to the cooling event. C15 (SIC from AMSR) is the coldest run with SIC of 100% throughout these two days. C15MOD (SIC from MODIS) is only slightly warmer. The warmest run is C15MOD0, which has a SIC of about 95% on January 27 and of about 90% on January 28. The effect of the daily restart is reflected by the jump in temperatures and SIC at 00 UTC. It should be kept in mind that 23 UTC is at the end of the 30 h forecast of CCLM and 00 UTC is a 6 h forecast initialized with different synoptic conditions. The C15MOD0h and C15MOD0htit runs are also very similar and simulated temperatures are between the C15 and C15MOD0 runs, which reflects the dominant influence of the SIC. In contrast, the ERA5 data show higher temperature values and a much weaker cooling.

Other interesting cases are shown in the supplementary material. For a cooling event associated with cloud-free conditions during February 14 and 15 (Figure S4a), the SIC is 100% for all simulations, but the C15MOD0 and C15MOD0h runs are several °C warmer than the C15 run, which indicates that advection from surrounding grid points is dominating. During the cloud-free period February 28–29 (Figure S4b), the observed temperature is almost constant at about –35°C, and the C15 run is up to 10°C colder than the observations. The C15MOD0 run is closest to the observations, and the temperature difference between the runs is dominated by the differences in SIC. A contrasting example is shown in Figure S5a for

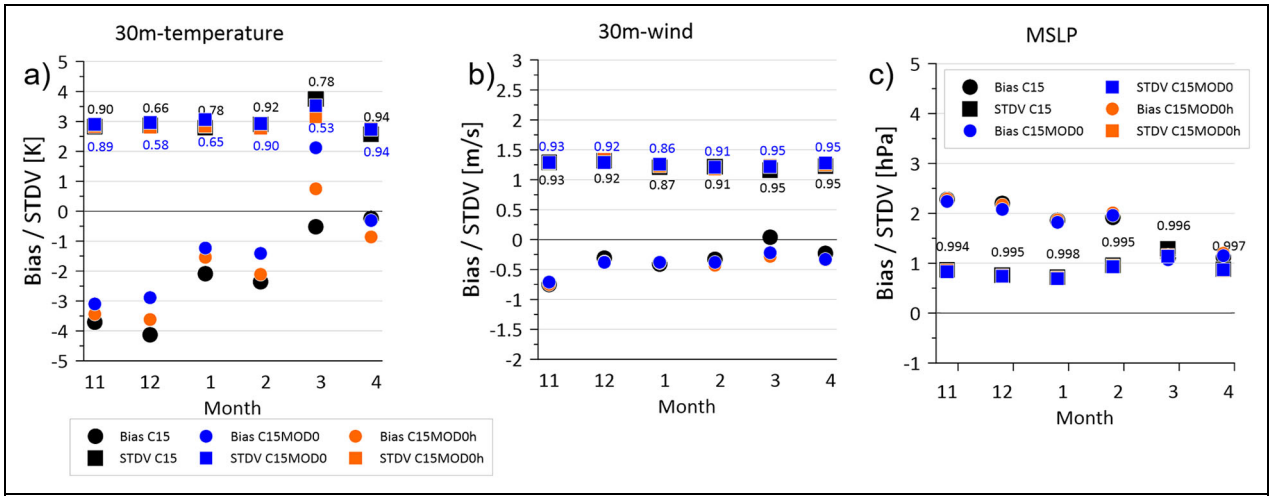

Figure 7. Comparison of simulations and Polarstern observations for monthly data. Bias (dots) and STDV (squares) for the comparison of C15 (black), C15MOD0 (blue), and C15MOD0h (orange) with Polarstern observations for November 2019 to April 2020 based on hourly data. Correlation coefficients (detrended data) for each month are shown as labels at the STDV data. (a) 30-m temperature, (b) 30-m wind, (c) mean sea level pressure (correlation coefficients are almost identical for all CCLM runs).

the beginning of March, when exceptional high lead fractions are present (see **Figure 3**). While there is a large underestimation of the temperature by C15 on March 2 and 3, the C15MOD0 run is closest to the observations. This changes on March 4 and 5, when the C15MOD0 run is much too warm. The reason is the very low SIC, which is even below 70%, so that the grid point is treated as a polynya, where the grid-scale ice thicknesses is reduced in the model (see **Table 4**). Again, there are mostly cloud-free conditions on March 4 and 5 in observations and simulations. Low clouds are present on March 6 and all simulations of the temperature are close to the observations. On April 7 (Figure S5b), SIC in C15 is slightly lower than for C15MOD0, and all simulations are slightly too warm. On April 8, a cooling takes place under cloud-free conditions, which is overestimated by C15.

The situation on March 4 leading to the large difference of the C15MOD0 simulations compared to the observations is shown in Figure S6 for the composite of MODIS IST data and the daily average of the C15MOD0htit run. Polarstern is located in an area with scattered temperatures of about −30°C in the simulation. The MODIS IST are about 10°C colder in the Polarstern area, while higher temperatures similar to the simulation are present close to Greenland. A closer look at the area around Polarstern (Figure S7) shows many leads with a warm anomaly, but the IST in the leads is very low (about −30°C). This means that the leads are covered by relatively thick ice or their width is much less than the MODIS resolution. Taking the lead fraction for the computation of SIC for the simulations leads to the overestimation of the temperature for this situation.

It has to be noted, that all case studies show local conditions at the Polarstern position and that 3-dimensional effects like advection have to be considered for local changes. The relation of local SIC to the air temperature will be further discussed in Section 4.

3.1.2. Statistics for months and the winter season

The monthly statistics of the comparison of C15, C15MOD0 and C15MOD0h with Polarstern observations for November 2019 to April 2020 are shown in **Figure 7**. For this comparison, data were linearly detrended for the calculation of correlation coefficients (r). The standard deviation (STDV) is the de-biased RMSE. The temperature bias for C15 is largest in November and December (around −4°C). It decreases to around −2°C in January/February and is very small in March/April. A large improvement can be seen for C15MOD0 for November to February, where around 1°C higher temperatures compared to C15 are simulated. While the C15 and C15MOD0 runs have almost no bias in April, a large positive bias of 2°C occurs for C15MOD0 in March, which is caused by a few days with huge biases as discussed above. Temperatures of the C15MOD0h runs lie between C15 and C15MOD0 (except for April). The correlation coefficients for temperature are variable with highest values in April. The wind speed is simulated very well with almost no bias by all runs, and the STDV is smaller than 1.5 m/s in all simulations. The pressure bias is relatively large particularly for November–February, but correlations exceed 0.99. CCLM tends to simulate too high pressure during high pressure situations, which can be seen in **Figure 5** for the period January 21–27, while differences are small during cyclonic events.

The overall statistics of the comparisons for wind, temperature and downward shortwave radiation for the whole winter are presented in **Figure 8**. In addition, the results are shown for ERA5 data. As already seen in **Figure 7**, the C15MOD0 run including sea ice leads has a smaller bias for the temperature than C15. In contrast, ERA5 data show a relatively large positive bias of 2°C. Wind speed shows small negative biases of about 0.5 m/s for all models. Downward shortwave radiation (only for March and April) shows almost no bias for the CCLM runs and a negative

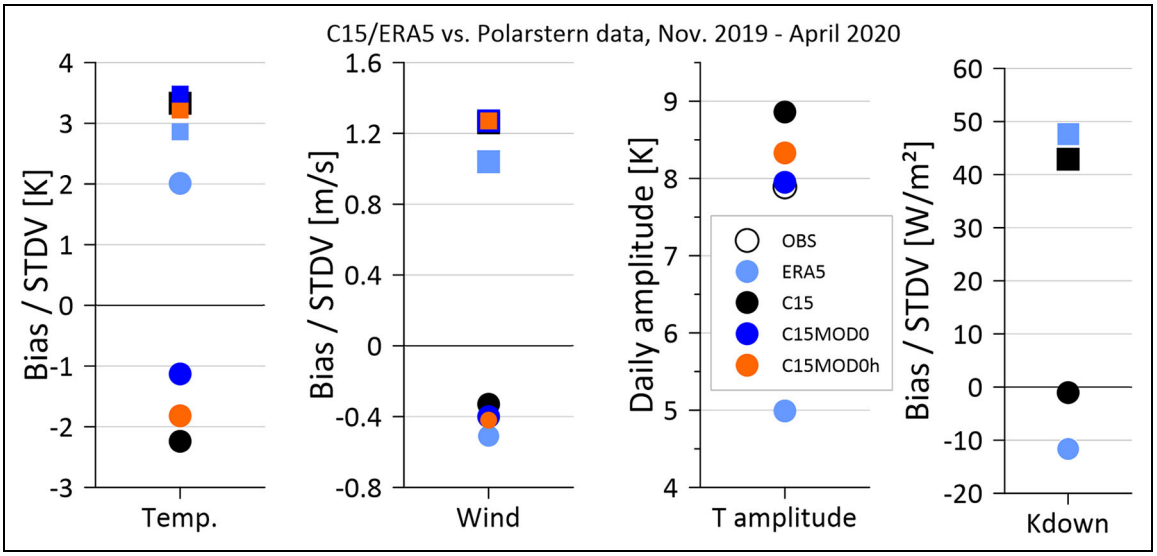

Figure 8. Comparison of simulations and Polarstern observations for the winter. Bias (dots) and STDV (squares) for the comparison of C15 (black), C15MOD0 (blue), and C15MOD0h (orange) and ERA5 (light blue) with Polarstern observations for November 2019 to April 2020 based on hourly data for 30m-temperature (Temp.), 30m-wind (Wind) and downward shortwave radiation (Kdown, values are almost identical for all CCLM runs). The temperature amplitude (T amplitude) is the difference between the 90% and 10% percentiles (after subtraction of the low-pass filtered time series, see text).

bias of about 10 W/m^2 for ERA5, but large STDV of 40–50 W/m^2 for all models. In order to quantify a mean daily temperature amplitude, the time series were low-pass filtered using a Gaussian filter with a filter width of 36 h. The low-pass filtered time series was then subtracted from the original time series, which yields a detrended time series with daily variations. As a measure of the mean daily amplitude the difference between the 90% and 10% percentiles of the daily variations was calculated. The simulated average temperature amplitude of C15 is about 1°C larger than the observations, C15MOD0h yields a slight improvement, and C15MOD0 reproduces the observations almost perfectly. In contrast, ERA5 largely underestimates the temperature amplitude by about 3°C.

3.2. Comparison of CCLM simulations with Met City observations

3.2.1. Statistics for months and the winter season

While the measurements from Polarstern meteorological system are performed routinely without special maintenance of the instruments, the tower and radiation measurements were supervised frequently during the experiment. The Met City data are available with only few short gaps during the whole winter period. Data at different levels, all 4 components of the radiation fluxes and turbulent fluxes were measured (see **Table 2**). Here, we focus on the 2-m temperature, the 10-m wind, and 2-m-specific humidity, which is a standard output of RCMs. It should be noted that these quantities are not at the model levels (see **Table 3**) and are interpolated in CCLM from the 5 m and 16 m (wind) and 5 m and surface values (temperature, specific humidity).

The comparison for the different months (**Figure 9**) shows that the temperature bias is slightly smaller than for the Polarstern data, and again the C15MOD0 run shows a reduced bias for November to February compared to C15. STDV and correlations are similar for Polarstern and tower data. The overestimation of the temperature for March for C15MOD0 is even larger than for Polarstern data, while C15MOD0h reduces this bias considerably. The wind speed bias is very small (absolute values smaller than 0.5 m/s), and also the STDV is smaller than 1.5 m/s. The 2-m-specific humidity is underestimated for all runs particularly for November/December, and the absolute value of the bias is smaller than 0.1 g/kg for other months.

The comparison of the downward longwave radiation for different months (**Figure 10a**) shows an underestimation of 10–15 W/m^2 for November and December and only small biases for January to April (values are almost identical for all CCLM runs for downward radiation fluxes). STDV is between 20 and 30 W/m^2 and correlation coefficients are between 0.6 and 0.9. Downward shortwave radiation (**Figure 10b**) is only present for March and April and shows a small bias and correlation coefficients larger than 0.9. Absolute values of the net radiation bias (**Figure 10c**) are relatively small (around 5 W/m^2), STDV for the net radiation is between 15 and 20 W/m^2.

The overall statistics of the comparisons with Met City measurements for the whole winter are presented in **Figure 11**. In addition, the results are shown for ERA5 data. The C15MOD0 run improves the temperature bias by more than 1°C. ERA5 data show a relatively large positive bias of more than 2°C. Wind speed for CCLM runs shows very small negative biases of about –0.2 m/s, while ERA5 has a positive bias of around 0.5 m/s. The simulated average temperature amplitude of the CCLM runs is close to the observations, while ERA5 largely underestimates the temperature amplitude by more than 3°C. The statistics

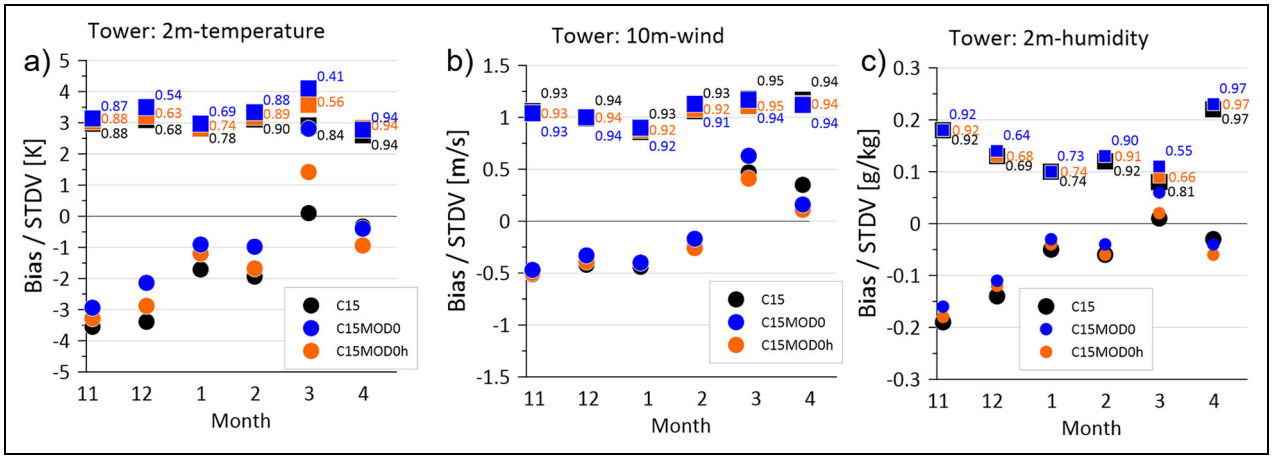

Figure 9. Comparison of simulations and tower observations for monthly data. Bias (dots) and STDV (squares) for the comparison of C15 (black), C15MOD0 (blue) and C15MOD0h (orange) with tower observations for November 2019 to April 2020 based on hourly data. Correlation coefficients (detrended data) for each month are shown as labels at the STDV data. (a) 2-m temperature, (b) 10-m wind, (c) 2-m-specific humidity.

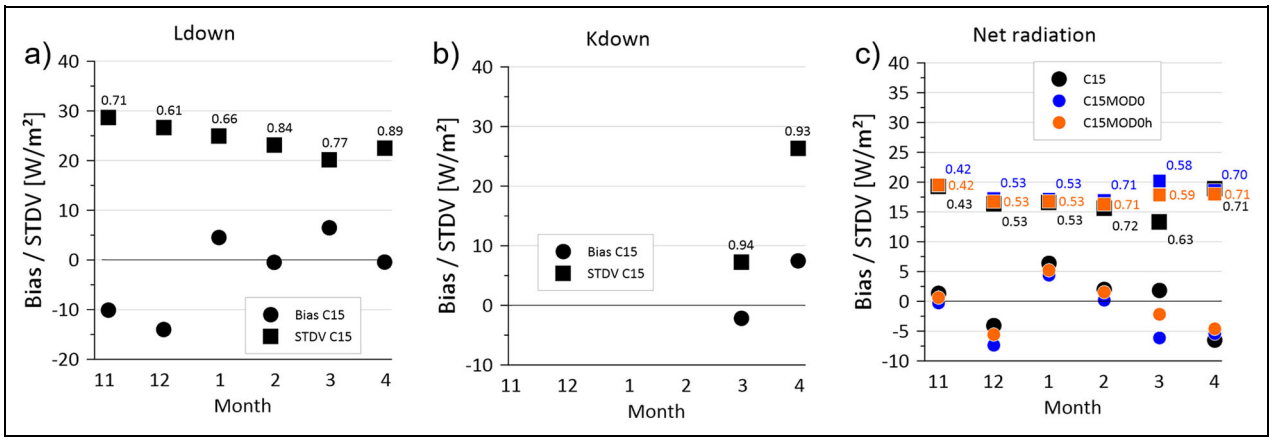

Figure 10. Comparison of simulations and Met City radiation observations for monthly data. Bias (dots) and STDV (squares) for the comparison of C15 with Met City observations for November 2019 to April 2020 based on hourly data. Correlation coefficients (detrended data) for each month are shown as labels at the STDV data. (a) downward longwave radiation (Ldown), (b) downward shortwave radiation (Kdown), (c) net radiation (C15MOD0 and C15MOD0h shown in addition). Net radiation is defined as the sum of net longwave radiation (L* = Ldown-Lup) and net shortwave radiation (K* = Kdown-Kup).

for the downward shortwave radiation show a small bias for the CCLM runs and ERA5, and STDV values of 20–25 W/m^2 for all models, which is much smaller than for the Polarstern data (this difference will be studied further in the next section). The bias for the downward longwave radiation is also small. The bias for the net radiation is close to zero for the CCLM runs, and slightly negative for ERA5. If only data of the months December to February are considered (Figure S8), the results are similar as for the whole winter period.

Figure 12 shows a more detailed view of the statistics of the comparison, including the frequency distribution of measured and simulated values as well as their differences. In general, CCLM has the tendency to slightly overestimate the frequency of temperatures larger than –20°C and smaller than −35°C (**Figure 12a**). The peak in the differences is in the range –2°C to 0°C, and there are only few cases with differences larger in magnitude than 6°C. In contrast, ERA5 strongly underestimates the frequency of temperatures below −30°C, while the frequencies of temperatures in the range −24°C to −20°C are strongly overestimated (**Figure 12c**). The peak in the differences is in the range 2°C–4°C. For wind, almost all speed ranges are simulated well by CCLM (**Figure 12b**), while ERA5 overestimates the frequency of wind speeds above 6 m/s and underestimates the frequency of weaker winds (**Figure 12d**).

3.2.2. Detailed study of radiation fluxes

The overall statistics for the shortwave radiation have shown large differences between the measurements at Met City (**Figure 11**) and Polarstern (**Figure 8**). These differences are also reflected in the frequency distributions, which show a huge range of differences, with some

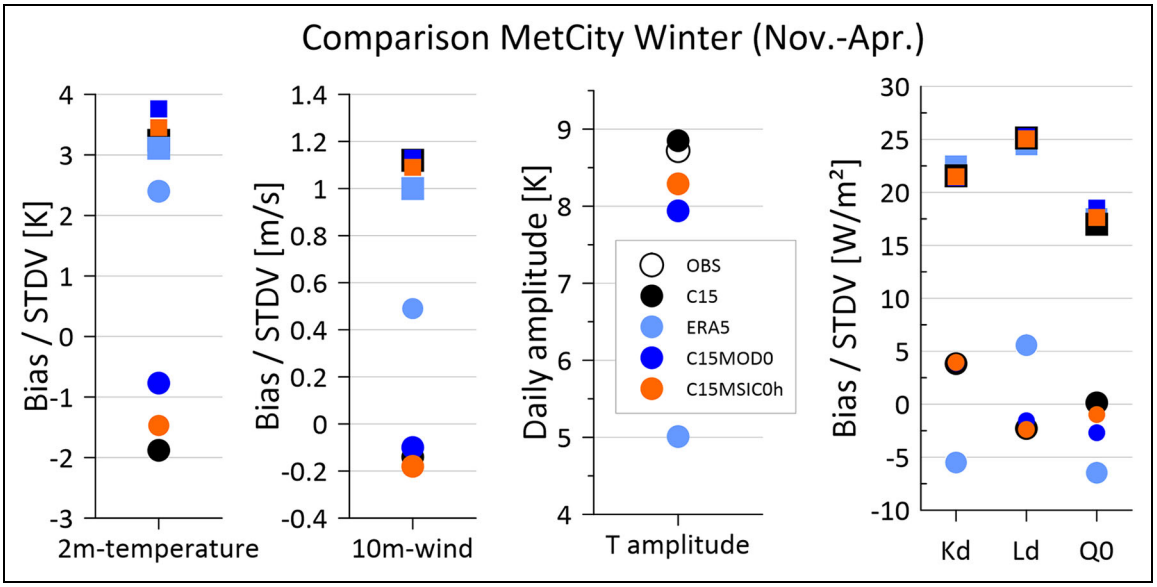

Figure 11. Comparison of simulations and Met City observations for the winter. Bias (dots) and STDV (squares) for the comparison of C15 (black), C15MOD0 (blue), C15MOD0h (orange) and ERA5 (light blue) with Met City observations for November 2019 to April 2020 based on hourly data for 2-m temperature, 10-m wind, downward shortwave radiation (Kd, only for March and April), downward longwave radiation (Ld) and net radiation (Q0). The temperature amplitude (T amplitude) is the difference between the 90% and 10% percentiles (after subtraction of the low-pass filtered time series).

more than 100 W/m^2, for the comparison with Polarstern data (**Figure 13b**). In contrast, differences compared to Met City data are generally smaller than 50 W/m^2 with a peak in the range ±20 W/m^2 (**Figure 13a**).

The differences for the downward shortwave radiation of Polarstern and Met City data can clearly be seen in the time series for April 2020 (**Figure 14**). Polarstern data are similar to the Met City data, but show much larger maxima for many days. This is particularly pronounced for the period April 21–27, 2020, which is a cloudless period (as indicated by the low values of the downward longwave radiation and the cloud base measurements, not shown). One likely reason for this effect is rime forming during the "night" on the pyranometer domes of the Polarstern instruments, which causes diffuse radiation on the sensor and leads to increased values. Since there is no maintenance for the Polarstern pyranometer, this effect is present until the rime has sublimated. The right subpanel of **Figure 14** supports this hypothesis, since a clear daily cycle of the temperature at 29 m is present, and the relative humidity typically exceeds 85%. Riming on the pyranometer was confirmed by the Polarstern webcam for April 25 and 26, but not for April 22–24. However, a disturbance by a nearby crane, reflections of the ship's exhaust-gas plume and reflections by the ship for certain solar zenith angles may also play a role in creating peaks in the pyranometer data. There was also shading by the ship superstructure for a few hours for very low sun elevation angles. The CCLM simulations of the downward shortwave radiation agree almost perfectly with the Met City data for this cloudless period.

The simulated downward longwave radiation for April 2020 (**Figure 14**) shows good agreement with the Met City data, while a slight underestimation occurs for some low values. This underestimation is likely caused by too little moisture in the lower troposphere, since the simulated downward longwave radiation is correlated with the integrated water vapor content of the lowest 2000 m (see below). In mid-April, 2 warming phases separated by a cooling event on April 16–18 occurred, which are also captured well by the CCLM simulations of the downward longwave radiation.

The distribution of the downward longwave radiation for the whole winter (**Figure 15a**) shows an overall good agreement with a slight underestimation by CCLM of the frequency of very low values. The majority of differences is in the range ±20 W/m^2. This comparison is similar for the net radiation (**Figure 15b**), where CCLM shows too many values below –60 W/m^2, but again an overall good agreement. When looking only at clear conditions, which are defined here as QCIT < 0.002 kg/m^2, the overestimation of the frequency of low Ldown values is more pronounced (Figure S9a), but also an underestimation of the frequency of values larger than 160 W/m^2 can be seen. The difference distribution (Figure S9b) shows the highest frequency at −10 to −20 W/m^2. The 2-m humidity difference for clear conditions (Figure S9c) shows the tendency for an underestimation (mean bias of 0.08 g/kg).

The downward longwave radiation is a main driver of the surface temperature during winter. **Figure 16** shows the dependence of the surface temperature (T_0) simulated by C15MOD0 on the simulated downward longwave radiation (Ld). These quantities are well correlated, and a drop to very low temperatures can be seen for Ld smaller than 140 W/m^2, which is even more pronounced for the C15 run (Figure S10). A similar behavior can be seen for the

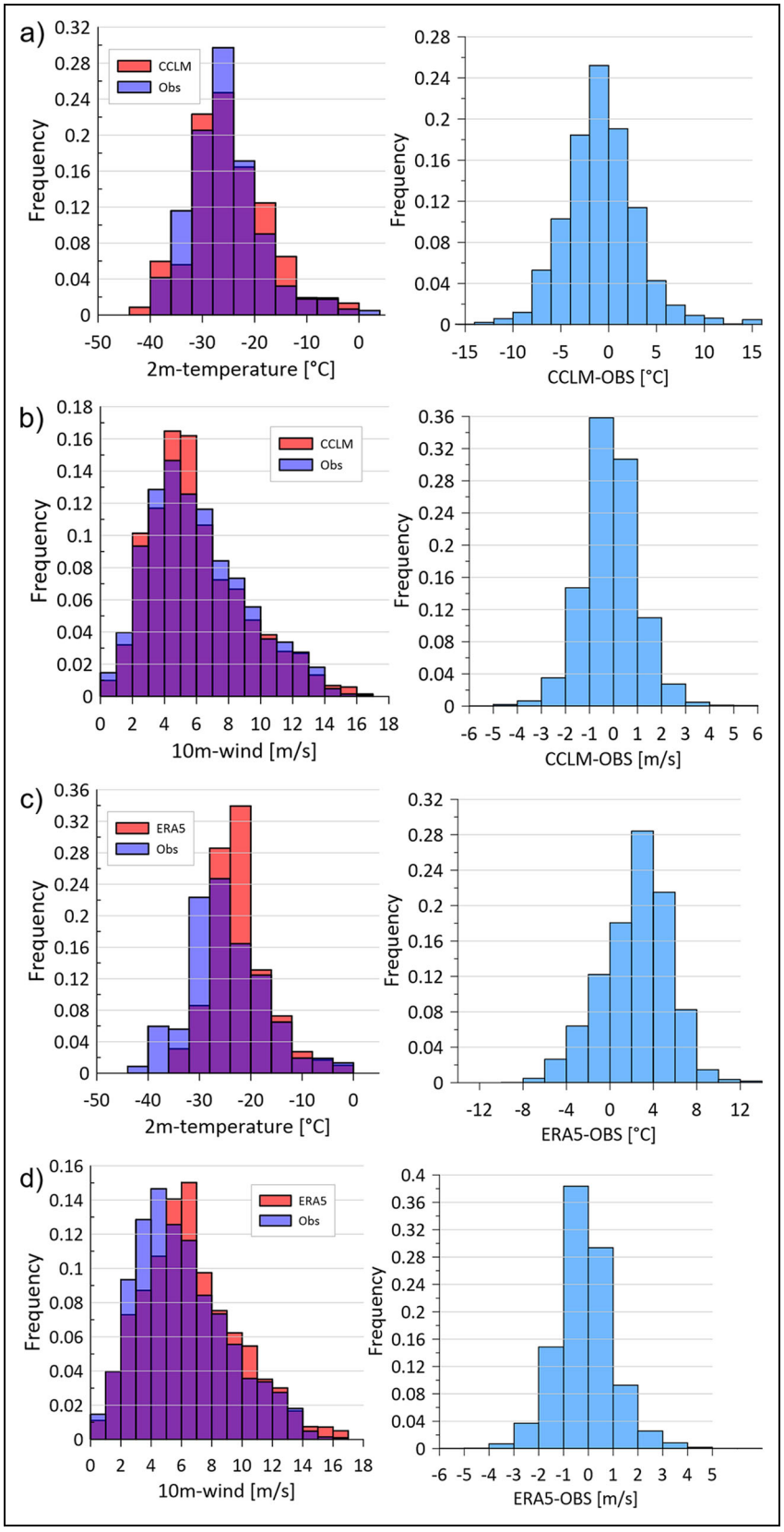

Figure 12. Frequency distributions of tower measurements and simulations for wind and temperature. Frequency distributions of measured (tower) and simulated values (1 h values) and their differences for C15MOD0 (a, b) and ERA5 (c, d) for November 2019 to April 2020: (a/c) 2-m temperature, (b/d) 10-m wind speed.

observations. This cooling occurs for clear-sky situations leading to a strong cooling of the snow layer. The regression shows a sensitivity of about 6 W/m^2/K. The scatter around the regression line is associated with the longwave radiation balance (color coded in **Figure 16**), again similar in CCLM and the observations. In ERA5, there is no snow

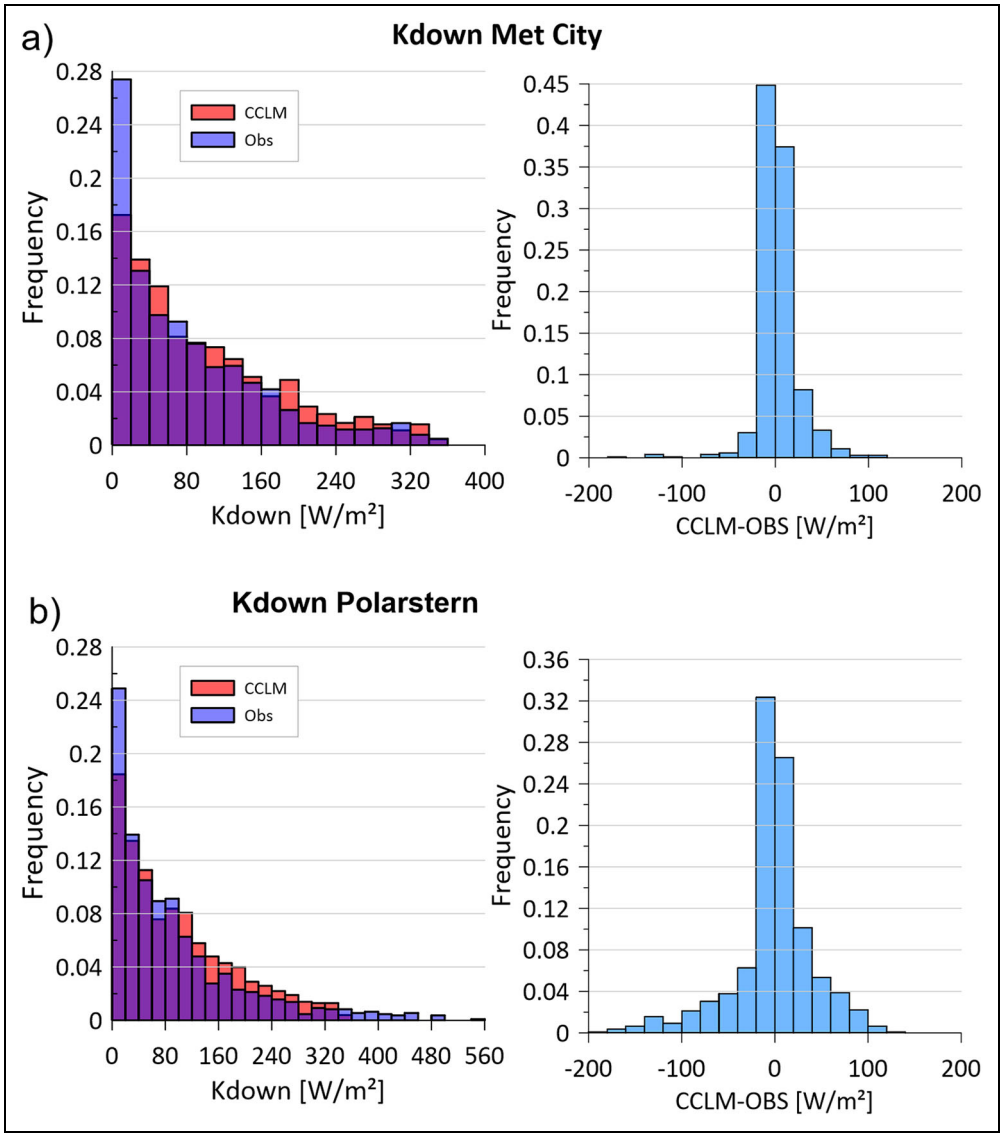

Figure 13. Frequency distributions of measurements and simulations for downward shortwave radiation. Frequency distributions of measured and simulated downward shortwave radiation (Kdown, 1 h values) and their differences for C15MOD0 for November 2019 to April 2020: for (a) Met City and (b) Polarstern data.

layer, and the surface temperature adapts more readily to the heat flux from the ice, which has a much larger inertia than the isolating snow layer. This leads to an underestimation of the sub-daily temperature variability (see **Figures 8** and **11**) and a warm bias.

The impact of the lower tropospheric humidity and temperature on the downward longwave radiation (Ld) is shown in **Figure 17**. The mean specific humidity (QL) and the mean temperature of the lowest 2000 m (TL) were computed from the hourly C15MOD0 profiles, since these quantities can be considered as the main factors for controlling Ld for conditions without low-level clouds. The presence of clouds is described by QCIT, and clear-sky conditions are assumed for QCIT < 0.002 kg/m^2. For cloudy conditions (**Figure 17a**), Ld is largely influenced by QCIT. For clear-sky conditions (**Figure 17b**), Ld is correlated to QL (slope of about 90 W/m^2/(g/kg). Ld is also correlated to TL (slope of about 4 W/m^2/K), but there is a large scatter for temperatures higher than –25°C, where Ld is dominated by QL. In conclusion, the underestimation of Ld of typically 20 W/m^2 for clear-sky conditions and low temperatures would correspond to an underestimation of TL by about 5°C or to an underestimation of QL by about 0.2 g/kg. This difference is in the range of the differences found when comparing the CCLM 2-m mixing ratio with the tower observations for clear-sky conditions (Figure S9).

4. Discussion

The data of MOSAiC offer new opportunities for the verification of RCMs, since there exist only few verification data sets over sea ice for the inner Arctic during winter. However, strong interactions of the atmosphere with the sea ice and ocean occur during winter, which have strong impacts on the ABL. The presence of SBL during winter over sea ice and sea ice leads are a challenge for the parameterizations of RCMs. The MOSAiC experiment covers a whole winter period for thick sea ice conditions and

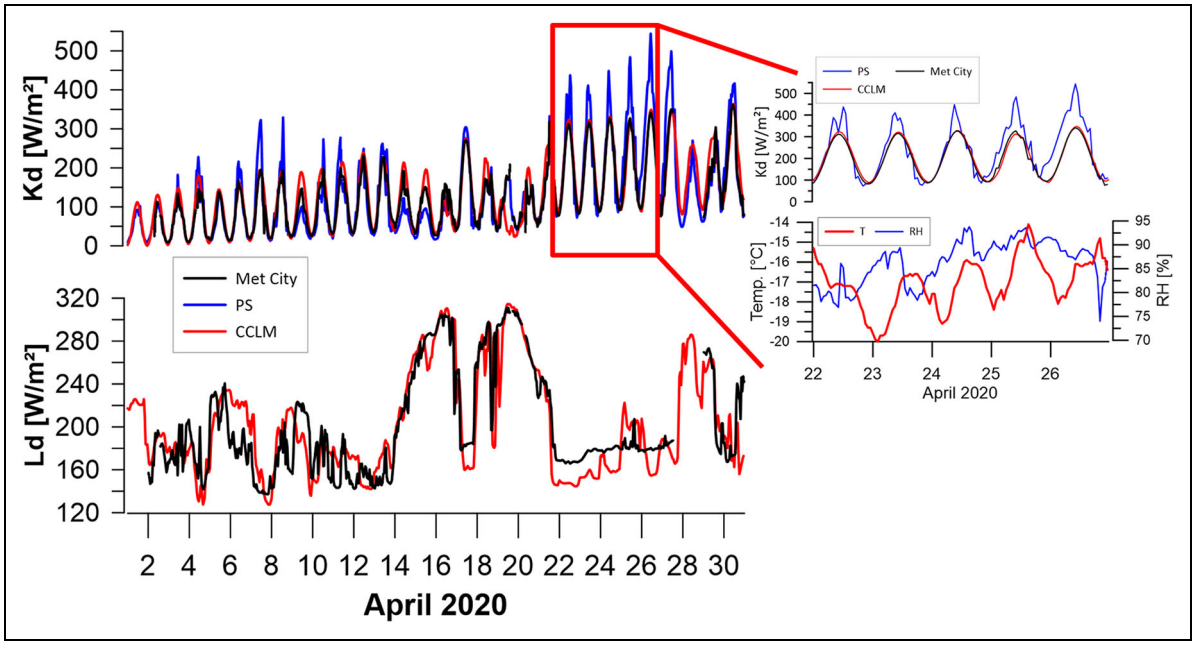

Figure 14. Comparison of downward radiation fluxes from measurements and simulations for April 2020. Downward shortwave radiation (Kd, top panel) and downward longwave radiation (Ld, lower panel) for April 2020 for the Met City data (black), Polarstern data (PS, blue), and CCLM simulations (red). The right panel shows the period April 22–26, 2020, with temperature and relative humidity (RH) of Polarstern observations in addition (all data are 1 h values).

is comparable only with the SHEBA campaign (1997–1998; Uttal et al., 2002), which was intensively used for model verification (Rinke et al., 2006).

A recent winter experiment for April 2019 for thick ice in the inner Arctic (Heinemann et al., 2021) was used for the verification and development of new ABL and sea ice parameterizations in CCLM, which led to the CCLM version used in the present study. They found a slight underestimation of the downward longwave radiation of 11 W/m^2, and a small positive bias in downward shortwave radiation (13 W/m^2), which are both in agreement with the present study, when comparing to the Met City data. For the 2-m temperature, they found a bias of –1.1°C and an RMSE of 2.5°C (corresponding to a STDV of 2.2°C). These results are comparable with the results of the present paper for April 2020, where a slight negative bias (–0.3°C) and a STDV of 2.6°C is found for C15. In contrast, large negative biases are present for November and December 2019.

For the net radiation, the emission of the surface and the surface albedo play an additional role. For the upward radiation fluxes (and albedo) it has to be taken into account that the measurements represent a specific ice floe, while the model represents a grid scale of 15 km, and ice conditions are different from reality (see below). This makes a comparison of upward radiation fluxes and net radiation more difficult compared to temperature and wind, where a blending of the influences of different surface types in the surroundings of the measurement site occurs. However, the net radiation has a bias of around ±5 W/m^2 for the winter months and almost zero for the winter mean, but has an RMSE of about 20 W/m^2.

The representation of sea ice is of large importance for the simulation of near-surface quantities during winter. The sea ice thickness for the grid-scale ice in our simulations is taken from PIOMAS data (Zhang and Rothrock, 2003). The development of the ice thickness along the Polarstern track for November 2019 to April 2020 is shown in **Figure 18a**. The data used in CCLM agree well with data of CryoSat/SMOS observations (Ricker et al., 2017) within 25 km of Polarstern (Krumpen et al., 2021), but in situ measurements of the ice thickness on and near the MOSAiC floe yield much lower values. The in situ measurements T62 and T66 were taken at the ice coring sites on the floe (Lei et al., 2021). For November, the ice thickness at different positions on the floe measured about 0.4 m and 0.8 m, while our simulations assume an ice thickness of 1.2 m. The differences are similar for December, and it is likely that a too large ice thickness is the reason for the large negative temperature biases of CCLM for November and December 2019. When the ice thickness increases during the course of the winter (to about 1.5 m in the measurements in April) the effect of the difference in ice thickness gets smaller.

A second aspect of the sea ice representation is the consideration of the sea ice thickness on the sub-grid-scale of the model. As in most uncoupled RCMs, we use a tile approach with flux averaging according to SIC. Thin ice thickness (TIT) in the nonice fraction is computed by thermodynamic growth in our simulations, which is a more realistic approach than to assume open water because rapid sea ice formation occurs in winter leads. **Figure 18b** shows TIT in leads at the Polarstern grid point from C15MOD0 and C15MOD0htit as used for the

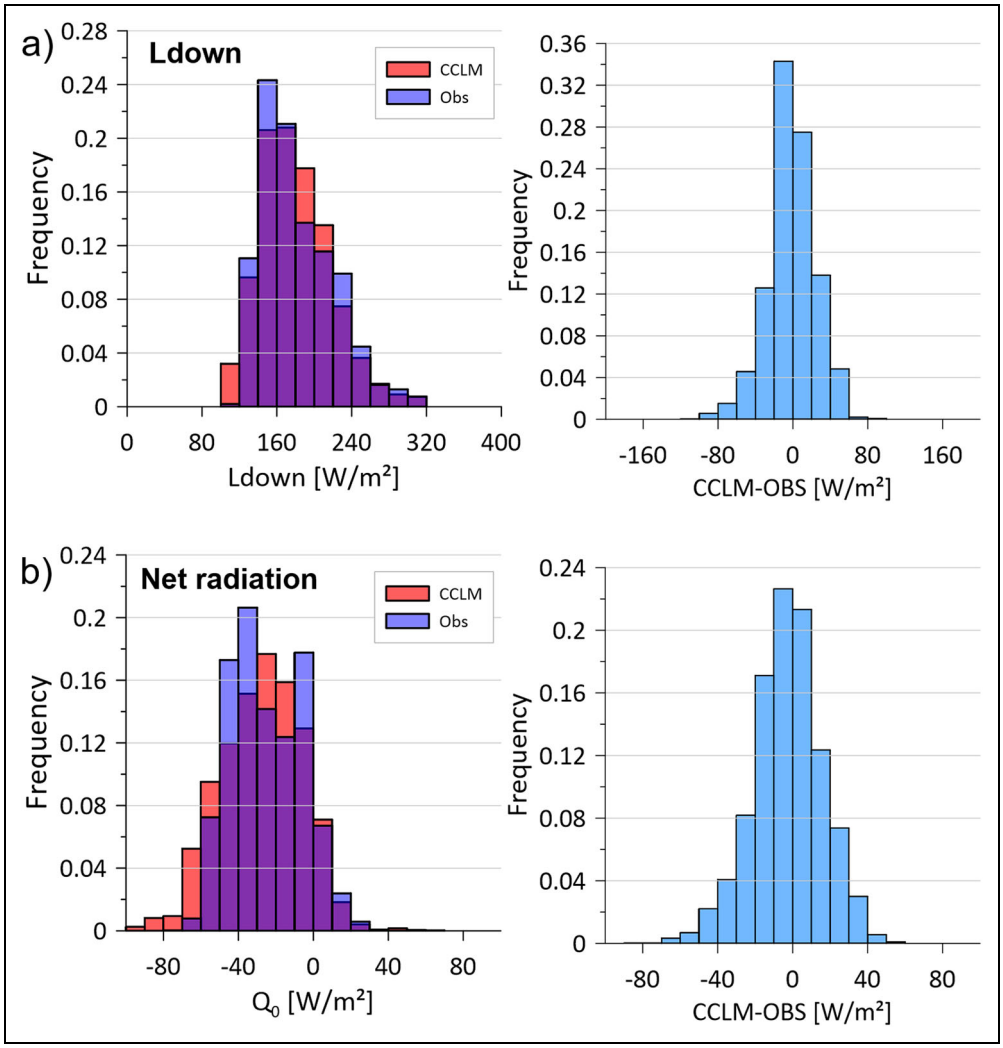

Figure 15. Frequency distributions of measurements and simulations for downward longwave radiation and net radiation. Frequency distributions of measured (Met City) and simulated radiation fluxes (1 h values) and their differences for C15MOD0 for November 2019 to April 2020: (a) downward longwave radiation (Ldown), (b) net radiation.

computation of sub-grid fluxes. The majority of TIT values is below 0.06 m for C15MOD0 and below 0.12 m for C15MOD0htit. As shown by Gutjahr et al. (2016) for polynyas, even a few centimeters of thin ice have a strong effect on the heat fluxes during winter. For the Polarstern grid point, the influence of doubling the TIT in C15MOD0htit has a small impact on the near-surface temperature in general.

A third aspect to consider is the representation of sea ice distribution and concentration. We find that using SIC including sea ice leads from MODIS data improves the simulation compared to the use of SIC from AMSR-E data by reducing the temperature bias by about 1°C. This effect is a result of the local sub-grid flux calculations, but advective effects from surrounding grid points play also a role. Since the fraction of leads in a 20 km radius around Polarstern is larger than 5% on many days during winter, the heat input to the atmosphere by leads is an important factor for the ABL (Lüpkes et al., 2008). This is demonstrated in **Figure 19**, which shows the frequency distribution of the SIC differences between the C15MOD0 and C15 (AMSR) runs (**Figure 19a**) and the IST differences (ΔT_0) against the differences in 5-m temperatures ($\Delta T5$ m, **Figure 19b**). SIC is the same for both runs about 60% of the time, but there are positive as well as negative values for the differences. The time series of SIC (Figure S11) shows that positive values (SIC from AMSR lower than for C15MOD0) occur mostly in the second half of April, but there are also cases in February and March. Negative values occur throughout the winter, but the peak of low SIC in C15MOD0 at the beginning of March is outstanding (Figure S11).

For situations when the air temperature is driven by the surface one would expect a good relation between ΔT_0 and $\Delta T5$ m (**Figure 19b**). This can be seen for positive and negative ranges (note that points overlap). The negative range (negative ΔT_0 and negative $\Delta T5$ m) is generally associated with positive ΔSIC, that is, SIC in C15MOD0 is larger than in C15. In the positive range IST differences larger than 5°C are also related to ΔSIC (SIC in C15MOD0 is smaller than in C15). However, there are many data points with a small difference in surface temperature, but

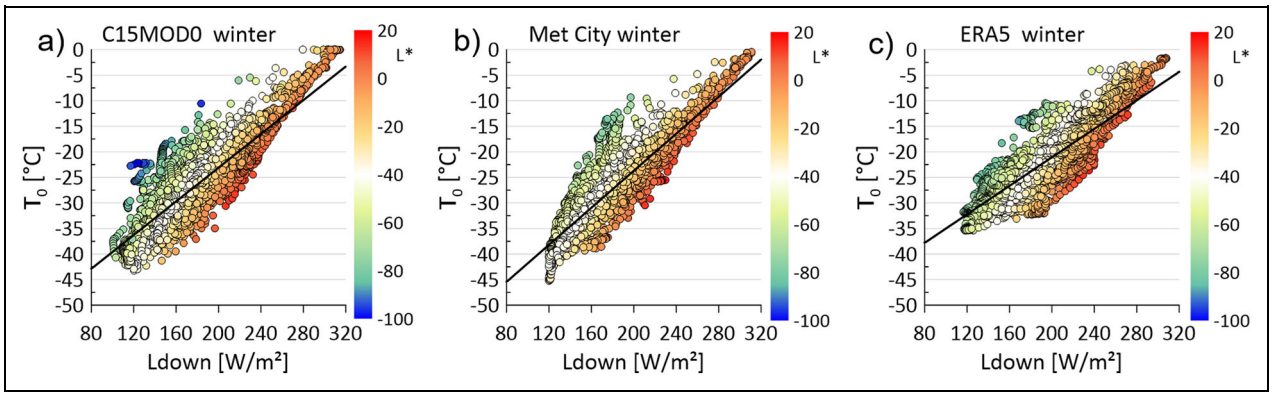

Figure 16. Scatter plots of surface temperature against downward longwave radiation. Scatter plots of the surface temperature against downward longwave radiation as simulated by (a) C15MOD0, (b) Met City data, and (c) ERA5. The color code is the net longwave radiation (in W/m^2). Full lines are the linear regressions of the respective data.

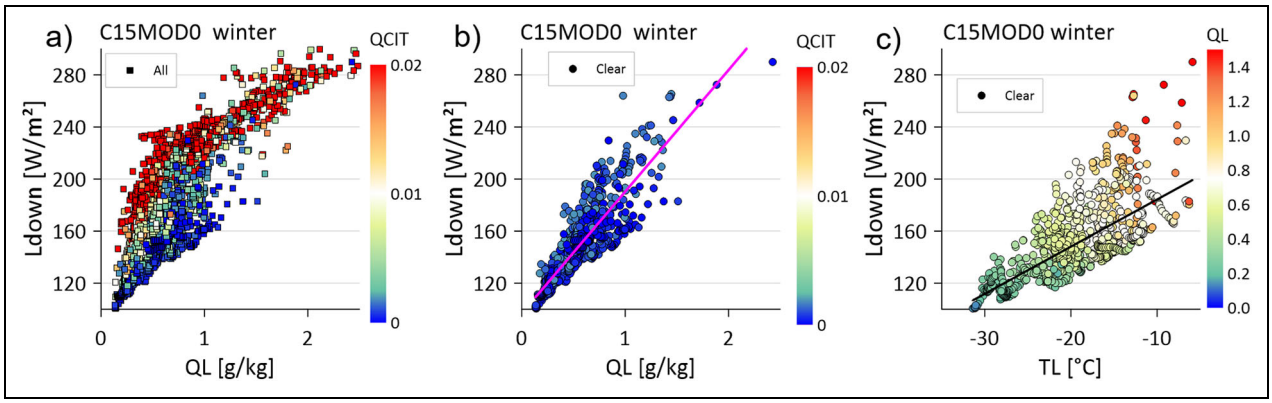

Figure 17. Scatter plots of downward longwave radiation against lower tropospheric humidity and temperature. Scatter plots of the downward longwave radiation as simulated by C15MOD0 against specific humidity (QL, a, b) and temperature (TL, c) for the lowest 2,000 m. (a) all data with the sum of cloud water and cloud ice color coded; (b) as (a) but only for clear conditions; (c) only clear conditions with QL color coded. Full lines are the linear regressions of the respective data.

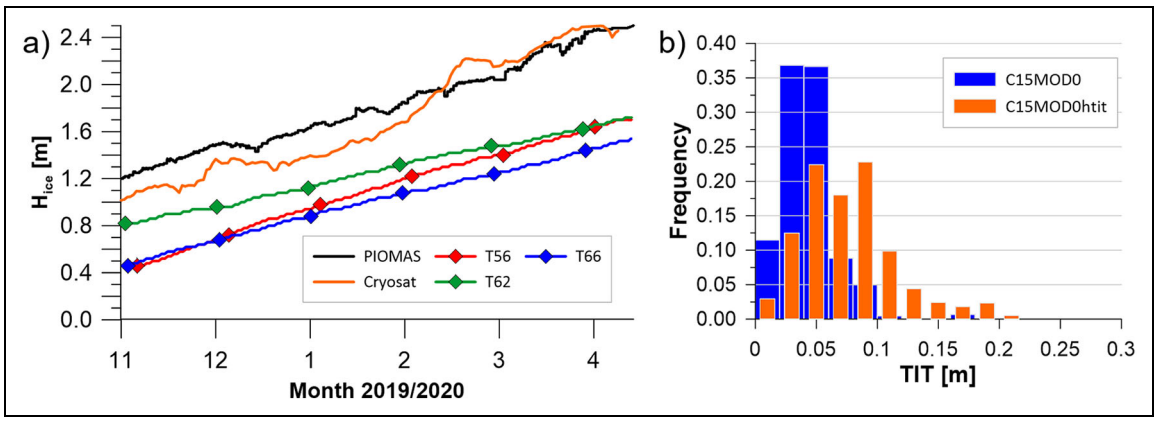

Figure 18. Sea ice thickness as used by CCLM and measured data. (a) Grid-scale sea ice thickness as used by CCLM (daily PIOMAS data) for the grid point of Polarstern, daily CryoSat/SMOS data from (Krumpen et al., 2021), daily in situ measurements of the ice thickness at different positions on (T62, T66) and near (T56) the MOSAiC floe (Lei et al., 2021); (b) frequency distribution of sub-grid-scale thin ice thickness (TIT, computed daily) for the grid point of Polarstern for C15MOD0 and C15MOD0htit for November 2019 to April 2020.

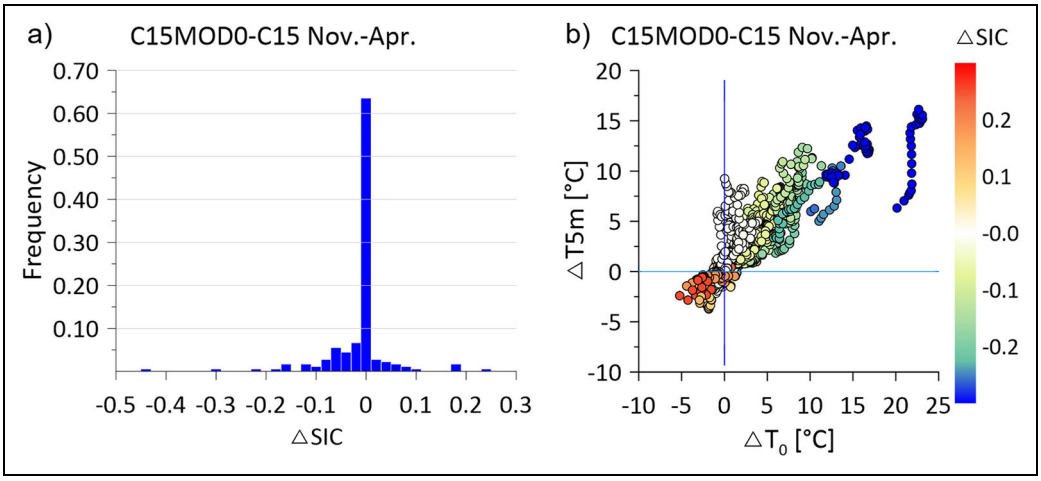

Figure 19. Frequency distribution of SIC differences and scatter plot of IST and air temperature differences for the grid point of Polarstern. (a) Frequency distribution of the SIC differences between the C15Mod0 and the C15 run (bins of 0.02). (b) Scatter plot of IST and 5-m temperature differences between the C15MOD0 and the C15 run (hourly data, SIC difference color coded).

a large difference in air temperature, which indicates that temperature advection is present.

The C15MOD0 runs that use the MODIS lead fraction (LF) for SIC have shown that there are situations like for March 4, 2020, when the SIC gets too small resulting in an unrealistic high air temperature. This can occur, if a thermal anomaly of leads in MODIS IST is present (so they are detected as leads), but the IST in the leads is very low (–30°C). Thus it is likely that these leads are smaller than the MODIS resolution, and the use of the LF results in an underestimation for the SIC. As a consequence, an improvement of the lead product from MODIS seems to be necessary. One approach could be to provide the IST and the background temperature of thick ice for each lead pixel. This would allow for a variable weight of the use of the LF for the SIC in the model depending on the IST and its anomaly in leads.

Besides the representations of the sea ice characteristics the ABL, parameterizations are also important. Our CCLM version uses a turbulence scheme for the SBL that was adapted to yield a better representation of the near-surface temperature and the SBL structure over polar ice sheets (Heinemann, 2020; Zentek and Heinemann, 2020). The modifications in the sea ice model and the tile approach (see **Table 5**) introduced by Heinemann et al. (2021) resulted in a good agreement with observations over sea ice. The present study confirms this finding for the MOSAiC data for the whole winter, but there is the tendency of the model to produce too low temperatures during clear-sky cooling phases.

5. Summary and conclusions

Measurements of near-surface variables during a whole winter period in the inner Arctic have been performed during MOSAiC. The state-of-the-art RCM CCLM with 15 km horizontal resolution was evaluated using measurements from the Polarstern meteorological system and at Met City near the ship. The impact of using MODIS-derived sea ice lead distributions was investigated. The main conclusions from this study are as follows:

- CCLM simulations show good agreement with the measurements for the near-surface variables for the whole winter (negative biases of 1°C–2°C for temperature, –0.2 m/s for wind speed). Relatively large negative biases of 3°C–4°C for temperature occur for November and December, which are likely associated with a too large ice thickness used by CCLM.
- The inclusion of a snow layer on the sea ice is essential for the representation of the sub-daily surface temperature variability. As most reanalyzes such as ERA5 assume a constant ice thickness without a snow layer, the surface temperature variability is underestimated and a warm bias occurs (Batrak and Müller, 2019).
- A tile approach should be used to consider sub-grid fluxes over sea ice. The sub-grid parameterization should account for thin ice in leads and polynyas.
- The use of MODIS-derived sea ice lead distributions improves model temperature biases but can lead also to an unrealistic warming for a few cases. An improvement of the sea ice lead product for the use in models is necessary.
- Radiation fluxes are generally represented well by CCLM (biases of ± 5 W/m^2), while an underestimation is found for very low values of the downward longwave radiation, which is likely related to an underestimation of the humidity of the lower troposphere. The use of shortwave fluxes from the Polarstern meteorological system is not recommended, if riming conditions or disturbances by the ship are possible.

MOSAiC observations represent a valuable dataset for the inner Arctic during winter. These data will be used in

the future by the MOSAiC consortium and other groups for the verification of state-of-the-art RCMs, weather forecast, and process models.

Data accessibility statement

The observational data will be made publicly available prior to January 1, 2023, on the MOSAiC archives. The Met City data of near-surface meteorology and surface energy flux measurements from the University of Colorado/NOAA surface flux team are available through the Arctic Data Center (arcticdata.io, Cox et al., 2021, and in part from the DOE Atmospheric Radiation Measurement Program archive (Riihimaki, 2021). Polarstern data are available by dship.awi.de/Polarstern.html. Model data are available on PANGAEA (https://doi.org/10.1594/PANGAEA.944502). ERA5 data are available on the Copernicus Climate Change Service (C3 S) Climate Data Store. https://cds.climate.copernicus.eu/#!/search?text=ERA5&type=dataset. MODIS data are available at https://nsidc.org/data/MOD29/versions/6 (accessed on January 3, 2022).

Supplementary files

The supplemental files for this article can be found as follows:

Figures S1–S11. Docx

Acknowledgments

Data used in this manuscript were produced as part of the international Multidisciplinary drifting Observatory for the Study of the Arctic Climate (MOSAiC) with the tag MOSAiC20192020 and the Project_ID: AWI_PS122_00. Meteorological data from Met City were provided by the University of Colorado / NOAA surface flux team. Radiation data from Met City were obtained from the Atmospheric Radiation Measurement (ARM) User Facility, a U.S. Department of Energy (DOE) Office of Science User Facility Managed by the Biological and Environmental Research Program. AWI (Holger Schmithüsen) provided the Polarstern data. We thank all those who contributed to MOSAiC and made this endeavor possible (Nixdorf et al., 2021).

Thanks go to the CLM Community and the German Meteorological Service for providing the basic COSMO-CLM model. This work used resources of the Deutsches Klimarechenzentrum (DKRZ) granted by its Scientific Steering Committee (WLA) under project ID bb0474. We acknowledge the use of imagery from the NASA Worldview application (https://worldview.earthdata.nasa.gov), part of the NASA Earth Observing System Data and Information System (EOSDIS). We thank the NSIDC for providing the MODIS IST data. The production of the merged CryoSat-SMOS sea ice thickness v2.3 data was funded by the ESA project SMOS & CryoSat-2 Sea Ice Data Product Processing and Dissemination Service, data for this manuscript were provided by Stefan Hendricks (AWI). In situ measurements of the ice thickness were provided by Lei et al. (2021). Model data processing was done with Climate Data Operators (CDO) (https://doi.org/10.5281/zenodo.3539275). Statistics were computed using the R software and the R package pracma.

Funding

This research was funded by the Federal Ministry of Education and Research (BMBF) under grant 03F0887A in the frame of the MOSAiC project "Modeling the impact of sea-ice leads on the atmospheric boundary layer during MOSAiC (MISLAM)." MDS was supported by the DOE Atmospheric System Research Program (DE-SC0021341), the National Science Foundation (OPP-1724551), and the NOAA Physical Sciences Laboratory and Global Ocean Monitoring and Observing Program. The publication was funded by the Open Access Fund of the University of Trier and the German Research Foundation (DFG) within the Open Access Publishing funding program.

Competing interests

The authors have declared that no competing interests exist.

Author contributions

Contributed to conception and design: GH.

Contributed to acquisition of data: SW, LS, MDS.

Contributed to analysis and interpretation of data: GH, MDS.

Drafted and/or revised the article: All authors.

Approved the submitted version for publication: All authors.

References

Andreas, EL. 1987. A theory for the scalar roughness and the scalar transfer coefficients over snow and sea ice. *Boundary-Layer Meteorology* **38**(1-2): 159–184. DOI: https://doi.org/10.1007/BF00121562.

Batrak, Y, **Müller, M.** 2019. On the warm bias in atmospheric reanalyses induced by the missing snow over Arctic sea-ice. *Nature Communications* **10**(1): 4170. DOI: https://doi.org/10.1038/s41467-019-11975-3.

Bauer, M, **Schröder, D**, **Heinemann, G**, **Willmes, S**, **Ebner, L.** 2013. Quantifying polynya ice production in the Laptev Sea with the COSMO model. *Polar Research* **32**(1): 20922. DOI: https://doi.org/10.3402/polar.v32i0.20922.

Charnock, H. 1955. Wind stress on a water surface. *Quarterly Journal of the Royal Meteorological Society* **81**(350): 639–640. DOI: https://doi.org/10.1002/qj.49708135027.

Cox, C, **Gallagher, M**, **Shupe, M**, **Persson, O**, **Solomon, A**, **Blomquist, B**, **Brooks, I**, **Costa, D**, **Gottas, D**, **Hutchings, J**, **Osborn, J**, **Morris, S**, **Preusser, A**, **Uttal, T.** 2021. 10-meter (m) meteorological flux tower measurements (Level 1 Raw), multidisciplinary drifting observatory for the study of arctic climate (MOSAiC), central Arctic, October 2019 September 2020. DOI: https://doi.org/10.18739/A2VM42Z5F.

Doms, G, **Förstner, J**, **Heise, H**, **Herzog, HJ**, **Mironov, D**, **Raschendorfer, M**, **Reinhardt, T**, **Ritter, B**, **Schrodin, R**, **Schulz, JP**, **Vogel, G.** 2013. *A description of the nonhydrostatic regional COSMO-model. Part II. Physical parameterizations*. Offenbach, Germany: Deutscher Wetterdienst.

Drüe, C, **Heinemann, G.** 2004. High-resolution maps of the sea-ice concentration from MODIS satellite data. *Geophysical Research Letters* **31**(20). DOI: https://doi.org/10.1029/2004GL020808.

Edgar, AL. 1987. A theory for the scalar roughness and the scalar transfer coefficients over snow and sea ice. *Boundary-Layer Meteorology* **38**(1–2): 159–184. DOI: https://doi.org/10.1007/BF00121562.

Elvidge, AD, **Renfrew, IA**, **Weiss, AI**, **Brooks, IM**, **Lachlan-Cope, TA**, **King, JC.** 2016. Observations of surface momentum exchange over the marginal ice zone and recommendations for its parametrisation. *Atmospheric Chemistry and Physics* **16**(3), 1545–1563. DOI: https://doi.org/10.5194/acp-16-1545-2016.

Gutjahr, O, **Heinemann, G**, **Preußer, A**, **Willmes, S**, **Drüe, C.** 2016. Quantification of ice production in Laptev Sea polynyas and its sensitivity to thin-ice parameterizations in a regional climate model. *The Cryosphere* **10**(6): 2999–3019. DOI: https://doi.org/10.5194/tc-10-2999-2016.

Hall, DK, **Key, JR**, **Case, KA**, **Riggs, GA**, **Cavalieri, DJ.** 2004. Sea ice surface temperature product from MODIS. *IEEE Transactions on Geoscience and Remote Sensing* **42**(5): 1076–1087. DOI: https://doi.org/10.1109/TGRS.2004.825587.

Hall, DK, **Riggs, GA.** 2021. MODIS/terra sea ice extent 5-min l2 swath 1 km, Version 61. DOI: https://doi.org/10.5067/MODIS/MOD29.061.

Hastings, DA, **Dunbar, PK.** 1999. Global land one-kilometer base elevation (GLOBE) digital elevation model, documentation. Key to Geophysical Records Documentation (KGRD) (34): 1–147. Available at https://www.ngdc.noaa.gov/mgg/topo/report/globedocumentationmanual.pdf. Accessed 5 August 2020.

Hebbinghaus, H, **Heinemann, G.** 2006. LM simulations of the Greenland boundary layer, comparison with local measurements and SNOWPACK simulations of drifting snow. *Cold Regions Science and Technology* **46**(1): 36–51. DOI: https://doi.org/10.1016/j.coldregions.2006.05.003.

Heinemann, G. 2020. Assessment of regional climate model simulations of the katabatic boundary layer structure over Greenland. *Atmosphere* **11**(6): 571. https://doi.org/10.3390/atmos11060571.

Heinemann, G, **Willmes, S**, **Schefczyk, L**, **Makshtas, A**, **Kustov, V**, **Makhotina, I.** 2021. Observations and Simulations of meteorological conditions over arctic thick sea ice in late winter during the transarktika 2019 expedition. *Atmosphere* **12**(2): 174. DOI: https://doi.org/10.3390/atmos12020174.

Hersbach, H, **Bell, B**, **Berrisford, P**, **Hirahara, S**, **Horányi, A**, **Muñoz-Sabater, J**, **Nicolas, J**, **Peubey, C**, **Radu, R**, **Schepers, D**, **Simmons, A**, **Soci, C**, **Abdalla, S**, **Abellan, X**, **Balsamo, G**, **Bechtold, P**, **Biavati, G**, **Bidlot, J**, **Bonavita, M**, **Chiara, G**, **Dahlgren, P**, **Dee, D**, **Diamantakis, M**, **Dragani, R**, **Flemming, J**, **Forbes, R**, **Fuentes, M**, **Geer, A**, **Haimberger, L**, **Healy, S**, **Hogan, RJ**, **Hólm, E**, **Janisková, M**, **Keeley, S**, **Laloyaux, P**, **Lopez, P**, **Lupu, C**, **Radnoti, G**, **Rosnay, P**, **Rozum, I**, **Vamborg, F**, **Villaume, S**, **Jean-Noël, T**. 2020. The ERA5 global reanalysis. *Quarterly Journal of the Royal Meteorological Society* **146**(730): 1999–2049. DOI: https://doi.org/10.1002/qj.3803.

Inoue, J, **Sato, K**, **Rinke, A**, **Cassano, JJ**, **Fettweis, X**, **Heinemann, G**, **Matthes, H**, **Orr, A**, **Phillips, T**, **Seefeldt, M**, **Solomon, A**, **Webster, S.** 2020. Clouds and radiation processes in regional climate models evaluated using observations over the ice-free Arctic Ocean. *Journal of Geophysical Research: Atmospheres*. DOI: https://doi.org/10.1029/2020JD033904.

Knust, R. 2017. Polar research and supply vessel POLARSTERN operated by the Alfred-Wegener-Institute. *Journal of Large-Scale Research Facilities* **3**. DOI: https://doi.org/10.17815/jlsrf-3-163.

Kohnemann, SHE, **Heinemann, G.** 2021. A climatology of wintertime low-level jets in Nares Strait. *Polar Research* **40**. DOI: https://doi.org/10.33265/polar.v40.3622.

Kohnemann, SHE, **Heinemann, G**, **Bromwich, DH**, **Gutjahr, O.** 2017. Extreme warming in the Kara Sea and Barents Sea during the winter period 2000–16. *Journal of Climate* **30**(22): 8913–8927. DOI: https://doi.org/10.1175/JCLI-D-16-0693.1.

Køltzow, M. 2007. The effect of a new snow and sea ice albedo scheme on regional climate model simulations. *Journal of Geophysical Research: Atmospheres* **112**(D7). DOI: https://doi.org/10.1029/2006JD007693.

Krumpen, T, **Albedyll, L**, **Goessling, HF**, **Hendricks, S**, **Juhls, B**, **Spreen, G**, **Willmes, S**, **Belter, HJ**, **Dethloff, K**, **Haas, C**, **Kaleschke, L**, **Katlein, C**, **Tian-Kunze, X**, **Ricker, R**, **Rostosky, P**, **Rückert, J**, **Singha, S**, **Sokolova, J.** 2021. MOSAiC drift expedition from October 2019 to July 2020: Sea ice conditions from space and comparison with previous years. *The Cryosphere* **15**(8): 3897–3920. DOI: https://doi.org/10.5194/tc-15-3897-2021.

Lei, R, **Cheng, B**, **Hoppmann, M**, **Zuo, G.** 2021. Snow depth and sea ice thickness derived from the measurements of SIMBA buoys deployed in the Arctic Ocean during the Legs 1a, 1, and 3 of the MOSAiC campaign in 2019-2020. DOI: https://doi.org/10.1594/PANGAEA.938244.

Lüpkes, C, **Gryanik, VM.** 2015. A stability-dependent parametrization of transfer coefficients for momentum and heat over polar sea ice to be used in climate models. *Journal of Geophysical Research: Atmospheres* **120**(2): 552–581. DOI: https://doi.org/10.1002/2014JD022418.

Lüpkes, C, **Vihma, T**, **Birnbaum, G**, **Wacker, U.** 2008. Influence of leads in sea ice on the temperature of the atmospheric boundary layer during polar night. *Geophysical Research Letters* **35**(3). DOI: https://doi.org/10.1029/2007gl032461.

Mironov, D, **Ritter, B**, **Jan-Peter, S**, **Buchhold, M**, **Lange, M**, **MacHulskaya, E.** 2012. Parameterisation of sea and lake ice in numerical weather prediction models

of the German Weather Service. *Tellus A: Dynamic Meteorology and Oceanography* **64**(1): 17330. DOI: https://doi.org/10.3402/tellusa.v64i0.17330.

Nixdorf, U, **Dethloff, K**, **Rex, M**, **Shupe, M**, **Sommerfeld, A**, **Perovich, DK**, **Nicolaus, M**, **Heuzé, C**, **Rabe, B**, **Loose, B**, **Damm, E**, **Gradinger, R**, **Fong, A**, **Maslowski, W**, **Rinke, A**, **Kwok, R**, **Spreen, G**, **Wendisch, M**, **Herber, A**, **Hirsekorn, M**, **Mohaupt, V**, **Frickenhaus, S**, **Immerz, A**, **Weiss-Tuider, K**, **König, B**, **Mengedoht, D**, **Regnery, J**, **Gerchow, P**, **Ransby, D**, **Krumpen, T**, **Morgenstern, A**, **Haas, C**, **Kanzow, T**, **Rack, FR**, **Saitzev, V**, **Sokolov, V**, **Makarov, A**, **Schwarze, S**, **Wunderlich, T**, **Wurr, K**, **Boetius, A.** 2021. MOSAiC Extended Acknowledgement. DOI: https://doi.org/10.5281/ZENODO.5179738.

Perovich, DK. 2007. Light reflection and transmission by a temperate snow cover. *Journal of Glaciology* **53**(181); 201–210. DOI: https://doi.org/10.3189/172756507782202919.

Platonov, V, **Kislov, A.** 2020. High-resolution COSMO-CLM modeling and an assessment of mesoscale features caused by coastal parameters at near-shore arctic zones (Kara Sea). *Atmosphere* **11**(10): 1062. DOI: https://doi.org/10.3390/atmos11101062.

Preußer, A, **Ohshima, KI**, **Iwamoto, K**, **Willmes, S**, **Heinemann, G.** 2019. Retrieval of wintertime sea ice production in arctic polynyas using thermal infrared and passive microwave remote sensing data. *Journal of Geophysical Research: Oceans* **124**(8): 5503–5528. DOI: https://doi.org/10.1029/2019JC014976.

Reiser, F, **Willmes, S**, **Heinemann, G.** 2020. A new algorithm for daily sea ice lead identification in the Arctic and Antarctic winter from thermal-infrared satellite imagery. *Remote Sensing* **12**(12): 1957. DOI: https://doi.org/10.3390/rs12121957.

Ricker, R, **Hendricks, S**, **Kaleschke, L**, **Tian-Kunze, X**, **King, J**, **Haas, C.** 2017. A weekly Arctic sea-ice thickness data record from merged CryoSat-2 and SMOS satellite data. *The Cryosphere* **11**(4): 1607–1623. DOI: https://doi.org/10.5194/tc-11-1607-2017.

Riihimaki, L. 2021. *Radiation instruments on Ice (ICERA-DRIIHIMAKI)*. Atmospheric Radiation Measurement (ARM) user facility. DOI: https://doi.org/10.5439/1608608.

Rinke, A, **Dethloff, K**, **Cassano, JJ**, **Christensen, JH**, **Curry, JA**, **Du, P**, **Girard, E**, **Haugen, JE**, **Jacob, D**, **Jones, CG**, **Køltzow, M**, **Laprise, R**, **Lynch, AH**, **Pfeifer, S**, **Serreze, MC**, **Shaw, MJ**, **Tjernström, M**, **Wyser, K**, **Žagar, M.** 2006. Evaluation of an ensemble of arctic regional climate models: Spatiotemporal fields during the SHEBA year. *Climate Dynamics* **26**(5): 459–472. DOI: https://doi.org/10.1007/s00382-005-0095-3.

Ritter, B, **Geleyn, J-F.** 1992. A comprehensive radiation scheme for numerical weather prediction models with potential applications in climate simulations. *Monthly Weather Review* **120**(2): 303–325. DOI: https://doi.org/10.1175/1520-0493(1992)120<0303:ACRSFN>2.0.CO;2.

Rockel, B, **Will, A**, **Hense, A.** 2008. The regional climate model COSMO-CLM (CCLM). *Meteorologische Zeitschrift* **17**(4): 347–348. DOI: https://doi.org/10.1127/0941-2948/2008/0309.

Schröder, D, **Heinemann, G**, **Willmes, S.** 2011. The impact of a thermodynamic sea-ice module in the COSMO numerical weather prediction model on simulations for the Laptev Sea, Siberian Arctic. *Polar Research* **30**(1): 6334. DOI: https://doi.org/10.3402/polar.v30i0.6334.

Sedlar, J, **Tjernström, M**, **Rinke, A**, **Orr, A**, **Cassano, J**, **Fettweis, X**, **Heinemann, G**, **Seefeldt, M**, **Solomon, A**, **Matthes, H**, **Phillips, T**, **Webster, S.** 2020. Confronting arctic troposphere, clouds, and surface energy budget representations in regional climate models with observations. *Journal of Geophysical Research: Atmospheres* **125**(6). DOI: https://doi.org/10.1029/2019JD031783.

Shupe, MD, **Rex, M**, **Blomquist, B**, **Persson, P**, **Ola G**, **Schmale, J**, **Uttal, T**, **Althausen, D**, **Angot, H**, **Archer, S**, **Bariteau, L**, **Beck, I**, **Bilberry, J**, **Bucci, S**, **Buck, C**, **Boyer, M**, **Brasseur, Z**, **Brooks, IM**, **Calmer, R**, **Cassano, J**, **Castro, V**, **Chu, D**, **Costa, D**, **Cox, CJ**, **Creamean, J**, **Crewell, S**, **Dahlke, S**, **Damm, E**, **Boer, G**, **Deckelmann, H**, **Dethloff, K**, **Dütsch, M**, **Ebell, K**, **Ehrlich, A**, **Ellis, J**, **Engelmann, R**, **Fong, AA.**, **Frey, MM**, **Gallagher, MR**, **Ganzeveld, L**, **Gradinger, R**, **Graeser, J**, **Greenamyer, V**, **Griesche, H**, **Griffiths, S**, **Hamilton, J**, **Heinemann, G**, **Helmig, D**, **Herber, A**, **Heuzé, C**, **Hofer, J**, **Houchens, T**, **Howard, D**, **Inoue, J**, **Hans-Werner, J**, **Jaiser, R**, **Jokinen, T**, **Jourdan, O**, **Jozef, G**, **King, W**, **Kirchgaessner, A**, **Klingebiel, M**, **Krassovski, M**, **Krumpen, T**, **Lampert, A**, **Landing, W**, **Laurila, T**, **Lawrence, D**, **Lonardi, M**, **Loose, B**, **Lüpkes, C**, **Maahn, M**, **Macke, A**, **Maslowski, W**, **Marsay, C**, **Maturilli, M**, **Mech, M**, **Morris, S**, **Moser, M**, **Nicolaus, M**, **Ortega, P**, **Osborn, J**, **Pätzold, F**, **Perovich, DK**, **Petäjä, T**, **Pilz, C**, **Pirazzini, R**, **Posman, K**, **Powers, H**, **Pratt, KA**, **Preußer, A**, **Quéléver, L**, **Radenz, M**, **Rabe, B**, **Rinke, A**, **Sachs, T**, **Schulz, A**, **Siebert, H**, **Silva, T**, **Solomon, A**, **Sommerfeld, A**, **Spreen, G**, **Stephens, M**, **Stohl, A**, **Svensson, G**, **Uin, J**, **Viegas, J**, **Voigt, C**, **Peter von der, G**, **Wehner, B**, **Welker, JM**, **Wendisch, M**, **Werner, M**, **Xie, Z**, **Yue, F**. 2022. Overview of the MOSAiC expedition—atmosphere. *Elementa: Science of the Anthropocene* **10**(1). DOI: https://doi.org/10.1525/elementa.2021.00060.

Souverijns, N, **Gossart, A**, **Demuzere, M**, **Lenaerts, JTM**, **Medley, B**, **Gorodetskaya, IV**, **Vanden BS**, **Van Lipzig, NPM**. 2019. A new regional climate model for POLAR-CORDEX: Evaluation of a 30-year hindcast with COSMO-CLM 2 over Antarctica. *Journal of Geophysical Research: Atmospheres* **124**(3): 1405–1427. DOI: https://doi.org/10.1029/2018JD028862.

Spreen, G, **Kaleschke, L**, **Heygster, G**. 2008. Sea ice remote sensing using AMSR-E 89-GHz channels.

Journal of Geophysical Research: Atmospheres **113**(C2). DOI: https://doi.org/10.1029/2005JC003384.

Steger, C, **Bucchignani, E**. 2020. Regional climate modelling with COSMO-CLM: History and perspectives. *Atmosphere* **11**(11): 1250. DOI: https://doi.org/10.3390/atmos11111250.

Uttal, T, **Curry, JA**, **Mcphee, MG**, **Perovich, DK**, **Moritz, RE**, **Maslanik, JA**, **Guest, PS**, **Stern, HL**, **Moore, JA**, **Turenne, R**, **Heiberg, A**, **Serreze, MC**, **Wylie, DP**, **Persson, OG**, **Paulson, CA**, **Halle, C**, **Morison, JH**, **Wheeler, PA**, **Makshtas, A**, **Welch, H**, **Shupe, MD**, **Intrieri, JM**, **Stamnes, K**, **Lindsey, RW**, **Pinkel, R**, **Pegau, WS**, **Stanton, TP**, **Grenfeld, TC**. 2002. Surface heat budget of the Arctic Ocean. *Bulletin of the American Meteorological Society* **83**(2): 255–275. DOI: https://doi.org/10.1175/1520-0477(2002)083<0255:SHBOTA>2.3.CO;2.

Weiss, AI, **King, J**, **Lachlan-Cope, T**, **Ladkin, R**. 2011. On the effective aerodynamic and scalar roughness length of Weddell Sea ice. *Journal of Geophysical Research: Atmospheres* **116**(D19). DOI: https://doi.org/10.1029/2011JD015949.

Willmes, S, **Heinemann, G**. 2016. Sea-ice wintertime lead frequencies and regional characteristics in the arctic, 2003–2015. *Remote Sensing* **8**(1): 4. DOI: https://doi.org/10.3390/rs8010004.

Zentek, R. 2019. COSMO documentation (archived version from 2019, uploaded with permission of the DWD). DOI: https://doi.org/10.5281/ZENODO.3339384.

Zentek, R, **Heinemann, G**. 2020. Verification of the regional atmospheric model CCLM v5.0 with conventional data and lidar measurements in Antarctica. *Geoscientific Model Development* **13**(4): 1809–1825. DOI: https://doi.org/10.5194/gmd-13-1809-2020.

Zentek, R, Heinemann, G, **Sachs, E**. 2016. Climatology of wind, kinetic energy, and temperature spectra using a high-resolution climate model for Mid-Europe. *Journal of Climate* **29**(3): 963–974. DOI: https://doi.org/10.1175/JCLI-D-15-0540.1.

Zhang, J, **Rothrock, DA**. 2003. Modeling global sea ice with a thickness and enthalpy distribution model in generalized curvilinear coordinates. *Monthly Weather Review* **131**(5): 845–861. DOI: https://doi.org/10.1175/1520-0493(2003)131<0845:MGSIWA>2.0.CO;2.

How to cite this article: Heinemann, G, Schefczyk, L, Willmes, S, Shupe, MD. 2022. Evaluation of simulations of near-surface variables using the regional climate model CCLM for the MOSAiC winter period. *Elementa: Science of the Anthropocene* 10(1). DOI: https://doi.org/10.1525/elementa.2022.00033

Domain Editor-in-Chief: Detlev Helmig, Boulder AIR LLC, Boulder, CO, USA

Associate Editor: Paul B. Shepson, School of Marine and Atmospheric Sciences, Stony Brook University, Stony Brook, NY, USA

Knowledge Domain: Atmospheric Science

Part of an Elementa Special Feature: The Multidisciplinary Drifting Observatory for the Study of Arctic Climate (MOSAiC)

Published: August 3, 2022 **Accepted:** June 29, 2022 **Submitted:** February 24, 2022

ELEMENTA Science of the Anthropocene

Elem Sci Anth is a peer-reviewed open access journal published by University of California Press.

OPEN ACCESS